FABRICATION OF MAGNETIC NANOPILLARS AND X-RAY IMAGING OF SPIN-TRANSFER PHENOMENA

A DISSERTATION
SUBMITTED TO THE DEPARTMENT OF MATERIALS SCIENCE AND ENGINEERING
AND THE COMMITTEE ON GRADUATE STUDIES
OF STANFORD UNIVERSITY
IN PARTIAL FULFILLMENT OF THE REQUIREMENTS
FOR THE DEGREE OF
DOCTOR OF PHILOSOPHY

Scott Andrews
May 2005

I certify that I have read this dissertation and that, in my opinion, it is fully adequate in scope and quality as a dissertation for the degree of Doctor of Philosophy.

Bruce Clemens
(Principal Co-Advisor)

I certify that I have read this dissertation and that, in my opinion, it is fully adequate in scope and quality as a dissertation for the degree of Doctor of Philosophy.

Joachim Stöhr
(Principal Co-Advisor)

I certify that I have read this dissertation and that, in my opinion, it is fully adequate in scope and quality as a dissertation for the degree of Doctor of Philosophy.

Shan Wang

Approved for the University Committee on Graduate Studies.

Abstract

Spintronics has generated much interest and research in recent years. Conventional technology uses the electron charge to store and transmit information. Novel devices with additional functionalities can be made using the quantum mechanical spin in addition to the electron charge. Potential spintronic applications include spin transistors, quantum computers, and magnetic random access memory (MRAM). Currently, giant magnetoresistance read heads, which transmit information using spin polarized currents, are used extensively in the magnetic storage industry. MRAM has started to impact the storage industry with its recent introduction to the consumer market. It is expected to compete with flash memory, and, to a lessor extent, dynamic random access memory (DRAM). MRAM does not deteriorate with use like flash but both are nonvolatile. MRAM's relatively fast speed will allow it to compete with DRAM in applications where information needs to be stored without a continuous power supply. Since MRAM and other spintronic applications are dependent on the interaction of spin polarized currents with magnetic materials, this phenomenon deserves further investigation in order to gain a more complete understanding.

Spin-transfer torque, a magnetic phenomenon in which spin polarized currents can be used to alter the magnetic state of a ferromagnet. This torque can be used as the dominant switching mechanism in systems where the current density is high. However, at low current densities, this effect is overpowered by the Oersted field, the classical magnetic field created by an electric current. Unlike the spin-transfer torque which is proportional to the current density, the Oersted field is proportional to the total current. Thus, for the spin-transfer torque to be dominant, small structures are necessary. In an attempt to meet the design criteria of samples that would carry high

current density but low total current, holes were drilled with focused ion beam (FIB) into silicon nitride films and filled with a stack of two ferromagnets separated by a nonmagnetic spacer. These samples were analyzed using x-ray photoemission electron microspectroscopy (X-PEEM). Due to magnetic uniformity issues in these samples, two other structures were subsequently investigated. One uses a stencil method that allows easy variations of the exact materials chosen. However, this sample design has the disadvantage that the magnetic material that should be switched using the spin polarized currents is not localized to the pillar structure being tested. This creates extraneous GMR signals during electrical measurements. Another sample, which was fabricated with the help of Hitachi, was designed to isolate the magnetic materials to a small region and does not show the convolved signal during electrical measurements. Both of these samples were analyzed with a scanning transmission x-ray microscope (STXM). Using a pump-probe configuration, the time dependent effects of the spin-torque transfer were examined. In the last sample, spin-transfer torque, combined with conventional Oersted switching, was observed and analyzed. Such a direct observation of spin injection and its time characteristics has never been achieved previously.

Acknowledgements

This work would not have been possible without the contributions of many important people. My advisors Joachim Stöhr and Bruce Clemens not only guided me as to how to conduct effective research, but also taught me much as to what it means to be a good leader. Even when the initial experiments were difficult and not going as well as I had hoped, they provided invaluable encouragement and support. Hans Siegmann was an incredible mentor throughout my graduate career. I spent innumerable hours seeking his advice. He taught me to critically examine data and clarified my thinking as to how to turn theory into solid experiments. I also want to thank Shan Wang and Stacey Bent for guiding me in the final stages of the project and for serving on my orals committee. I also had the privilege to work with several scientists from IBM and Hitachi: Jordan Katine, Danielle Mauri, Charles Rettner, and Jan Thiele, all of whom helped with sample fabrication at various stages of my project. I am also deeply grateful to the Fannie and John Hertz Foundation for providing me the large majority of my financial support throughout my career.

Throughout my time at Stanford, the members of the Stöhr group were invaluable. Yves Acremann was an amazing inspiration. He is one of the most creative individuals I have ever known. He helped me to think in new ways and to constantly be looking for innovative ideas. Always underestimating his impact, Yves' guidance was one of the main forces that lead to this success of this project. I have spent more hours than I can count working with John Paul Strachan and Venkatesh Chembrolu. They have become great friends, and I could never have completed this project without their undying diligence and determination. The other scientists within the group and at the Advanced Light Source, Hendrik Ohldeg, Andreas Scholl, Christian Stamm, and

Tolek Tyliszczak, helped me immensely in my understanding of x-ray techniques and spent many hours showing me how to use incredibly complex instruments. I also want to thank Sara Gamble, Bill Schlotter, and Ioan Tudosa for their great companionship and comradery.

Unlike most graduate students, I had the privilege to work in two research groups. The Clemens group helped me immensely. Aditi Chandra, Guleid Hussen, Raj Kelekar, Yong-Won Lee, Gloria Wong, and I spent many hours discussing all aspects of science along with the far less technical issues of graduate school. I will always value the time shared with these great people.

Besides my those within my research groups, many other friends have been crucial. I want to especially thank Dan and Caroline Aubertine, Irene Chang, LuPei Chang, Brian and Caroline Chen, Ryan OHayre, Jeff Mason, Alan Lee, Dong-Ick Lee, Dong-Woon Shin, Lisa Wong, and all my other friends at Stanford who have kept me sane by reminding me that there is more to life than lab.

I also want to thank a good friend Kenneth Travers who, even though he is still back in Illinois, has continued to provide great advice and much inspiration. Also in Illinois, Jay Edwards and Jeff Visser have remained steadfast in their support even though many miles have separated us while I have been in California. Finally, and perhaps most importantly, I want to thank my parents who have always supported and encouraged me throughout my life.

Contents

List of Figures

Chapter 1

Models of spin injection

1.1 History

Until the twentieth century, only two methods were known for influencing magnetic structures. The first was discovered by the Chinese sometime during the Qin dynasty (221-206 B.C.), when lodestone was first used in fortune telling boards and later in compasses. In 1600 William Gilbert published *De Magnete*, which described the properties of magnetite, the chemical structure in lodestone, and related the earth's magnetic field to that produced by a magnet. For the next two hundred years, no one knew of an artificial method for influencing the magnetization of a material. Then in 1819 Hans-Christian Oersted accidentally brought a compass near a wire carrying a current and found that the compass needle was deflected. This allowed the second manipulation of magnetism: using currents to create magnetic fields. Recently, a third method was proposed and refined that would allow a magnet to select electrons of only one direction of spin and then use these electrons to manipulate ferromagnets through quantum interactions.

Before fully using quantum effects for manipulating magnetic structures, physicists had to develop models of the band structure within ferromagnetic and paramagnetic materials. By looking at the band structures, one finds that the magnetic character generally comes from the spin dependent asymmetry of the d-orbital, which is partially hybridized with the s- and p-orbitals. Band structure calculations for ferromagnets

show an unequal density of states for spin-up and spin-down electrons at the Fermi level, which gives rise to a net magnetic moment in the ground state.

Although these band structure calculations elucidated the causes of magnetism, greater insight into how current traveled within a ferromagnet was needed. In 1936 Mott [7, 8] published a paper detailing how current travels in two channels that weakly interact with each other. Although Mott neglected the phase relationship between the spin-up and spin-down components needed for a complete understanding [9] and the model was later expanded [10, 11], many technologically important aspects can be understood using this powerful model [12].

Following Mott's work, later experiments showed that the current stays polarized after exiting the ferromagnetic layer [13, 14, 15]. Although this initial work was generally done in the context of tunneling through an insulating layer and measuring photoemitted electrons, Aronov [16, 17, 18] proposed several key ideas for extending these findings into ferromagnet/paramagnet contacts. Aronov proposed that a nonequilibrium magnetization, or equivalently nonequilibrium spin accumulation, would be created in a region near the interface and decay away at a characteristic diffusion length. Johnson and Silsbee [19, 20] first measured such an effect in metals by using Silsbee's [21] idea of two ferromagnets sandwiched around a paramagnet. One ferromagnet serves to polarize the electrons while the other serves to detect the polarization.

Later experiments found the effects could be extended into ferromagnet / nonmagnetic / ferromagnetic heterostructures that displayed the spin-valve effect in the form of giant magnetoresistance (GMR) [22, 23], which is measured by the difference in the resistance between antiparallel (AP) and parallel (P) states of the two ferromagnetic layers.

$$GMR = \frac{R_{AP} - R_P}{R_P} \tag{1.1}$$

After room temperature GMR was discovered [24, 25], it was later incorporated into commercial disk drive read heads.

In order for magnetoresistance effects to be commercially viable, the relative orientation of the two ferromagnetic layers must be reliably controlled. Slonczewski [26] and Berger [27] proposed a novel method to control the relative magnetization. In their schemes, the polarized current leaving one ferromagnet can transfer angular momentum, often referred to as spin-transfer torque, to the other ferromagnetic layer, resulting in an alteration of the magnetization direction. Many researchers have continued to expand on this initial work [28, 29, 30, 31, 32]. Some of the most important work was done by Katine *et al.* [33], who were able to show spin induced switching at room temperature. Later, Albert *et al.* [2] were able to improve the signal by introducing shape anisotropy into the fabrication process.

1.2 Two Current Model

Mott's simple model [7, 8], which was later used as the basis for spin-transfer torque models, begins by defining the chemical potential for each species in the system. In this case, the relevant species are spin-up and spin-down electrons. In equilibrium they will have the same potential, but in cleverly designed non-equilibrium systems the two chemical potentials can be differentiated with some important applications.

One can define the electrochemical potential in the conventional way:

$$\bar{\mu}_j = \left(\frac{\partial G}{\partial N_j}\right)_{T,P,N_{i\neq j}} \tag{1.2}$$

where G is the Gibb's free energy, and N_j is the number of particles of species j. The outer subscripts emphasize that the partial derivative holds the temperature, pressure, and number of other species constant. Note that this equation includes any energy needed to add species j due to an applied electric field.

We can now examine the specific case of a ferromagnet in contact with a nonmagnetic material. Many researchers have examined this situation [34, 35, 12, 36, 37]. In the proper analysis, one must account for the differences in the Fermi distributions of spin-up and spin-down electrons created by the current flowing from a ferromagnet into a paramagnet. The distributions are altered because the relative densities of

spin-up and spin-down electrons at the interface are not the same in the ferromagnet and the paramagnet. Fortunately, several simplifications can be made in the majority of practical cases [12]. In order to highlight the major points without becoming lost in the details, we will examine the system using the simpler two current model.

When a ferromagnet comes into contact with a nonmagnetic material, the chemical potential of spin-up and spin-down electrons will equilibrate. When a current flows through the sample, Ohm's law must hold for each spin channel and the system as a whole.

$$\begin{aligned} \nabla\left(\tfrac{\sigma_\uparrow}{q}\mu_\uparrow\right) &= \vec{j}_\uparrow \\ \nabla\left(\tfrac{\sigma_\downarrow}{q}\mu_\downarrow\right) &= \vec{j}_\downarrow \\ \nabla\left(\tfrac{\sigma}{q}\mu_0\right) &= \vec{j} \end{aligned} \tag{1.3}$$

where $j_{\uparrow\downarrow}$ is the current density of the spin-up or spin-down channel. $j = j_\uparrow + j_\downarrow$ is the total current density. $\sigma_{\uparrow\downarrow}$ is the conductivity of each channel, and μ_0 is the electric potential within the system. Since spin flip scattering is relatively rare, it contributes little to the overall resistivity. As such, the total conductivity is simply the sum of the two channels: $\sigma = \sigma_\uparrow + \sigma_\downarrow$. Experiments by Fert and Campbell [11] suggest this is valid for Ni to at least room temperature. To simplify the above equations, the spin chemical potential $\bar{\mu}_{\uparrow\downarrow} \equiv \mu_{\uparrow\downarrow} - \mu_0$ can be introduced to yield

$$\nabla^2\left(\sigma_\uparrow\bar{\mu}_\uparrow + \sigma_\downarrow\bar{\mu}_\downarrow\right) = 0 \tag{1.4}$$

As will be shown shortly, these equations will lead to steady state condition in which the chemical potentials of the two channels are not equal. Thus, one channel contains more electrons than it does in equilibrium while the other channel has a deficit. When a spatial region contains a nonequilibrium population of spins, two processes act to bring the system into equilibrium: spin flips and diffusion. These are coupled by

$$\frac{\mu_\uparrow - \mu_\downarrow}{l_{sf}^2} = \nabla^2\left(\mu_\uparrow - \mu_\downarrow\right) \tag{1.5}$$

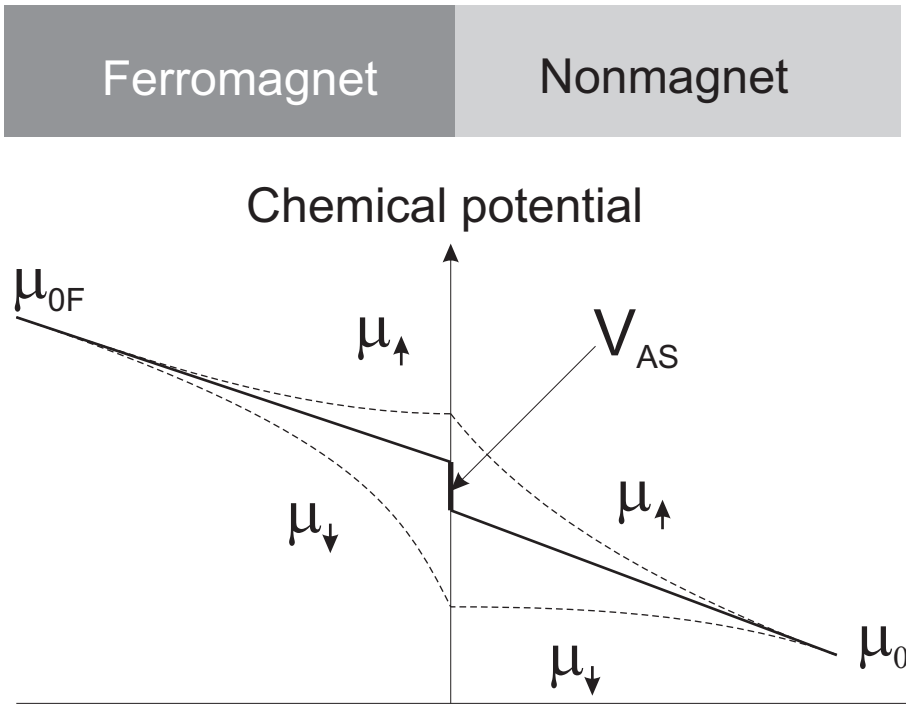

Figure 1.1: When current is passed though a ferromagnet / paramagnet interface, the discontinuity in the relative conductivities of each channel causes a divergence in which one spin is accumulated and the other is depleted relative to the ratio of spin-up and spin down electrons far from the interface. [1]

In the above equation, the diffusion coefficient and the spin flip time constant have been combined into the spin diffusion length l_{sf}.

Figure 1.1 shows the results of using equations 1.3 and 1.5. The spin channels have an equal electrochemical potential far from the interface. At the interface, each channel undergoes a sudden conductivity change. Since the conductivity changes are unequal, the two channels diverge. μ_0 is the weighted average of the electrochemical potentials and represents the electric potential that would be measured by a probe incapable of separating the two spin channels. This potential has a discontinuity, the spin accumulation voltage, at the interface due to the discontinuity in the ratio of $\sigma_\uparrow/\sigma_\downarrow$.

The voltage drop across the F/N interface mathematically produces the same result when analyzing the circuit as if the interface added a resistor to the circuit.

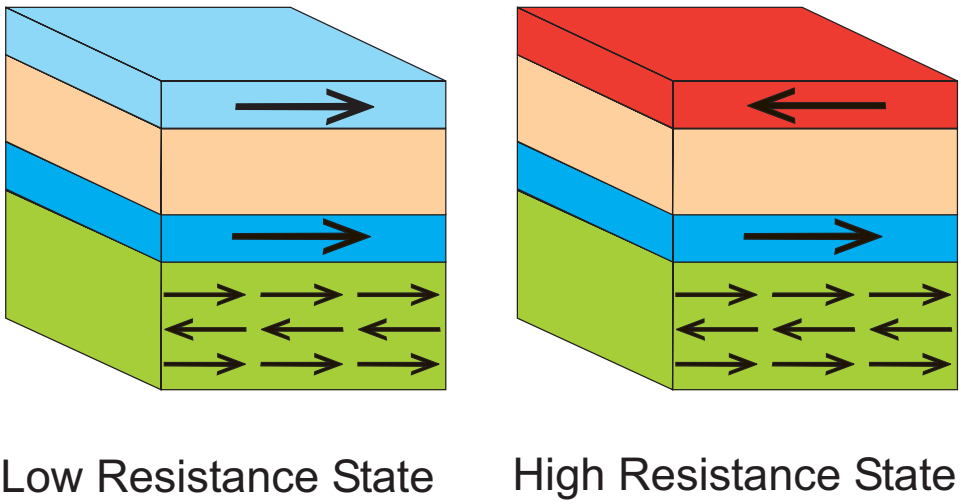

Figure 1.2: Spin valves are commonly used in hard drive read heads. The stray field from the bit transitions on the disk alters the magnetization direction of the top sensor layer. The lower layer is fixed using exchange biasing to an antiferromagnet. By passing current vertically through this stack and measuring the resistance, the state of the top layer can be determined. [1]

This boundary resistance is known as the giant magnetoresistance (GMR) effect. This effect is currently used commercially to make disk drive read heads. Figure 1.2 shows two states of a read head stack. The stray fields from the disk drive bit transitions alter the magnetization of the top layer of a F/N/F stack. The resistance of the stack is then measured to determine the relative orientation of the two magnetic layers. Figure 1.3 shows the spin chemical potential and the voltage drop at the two interfaces in the high and low resistance states. In the high resistance state, the spin accumulation voltages add and create a large effective resistance. However, in the low resistance state, the voltages partially cancel and create a lower total resistance. A typical GMR curve is shown in figure 1.4. In the sample shown, a pillar was created by Albert *et al.*. The two Co layers of a pillar structure have very different coercivities. At high positive fields, the layers are aligned and the resistance is low. After applying a small negative field, one layer switches and becomes antiparallel to the second layer. This results in a high resistivity state. At high negative fields, the two layers align and the resistance is low again. The reverse sweep shows the same effect.

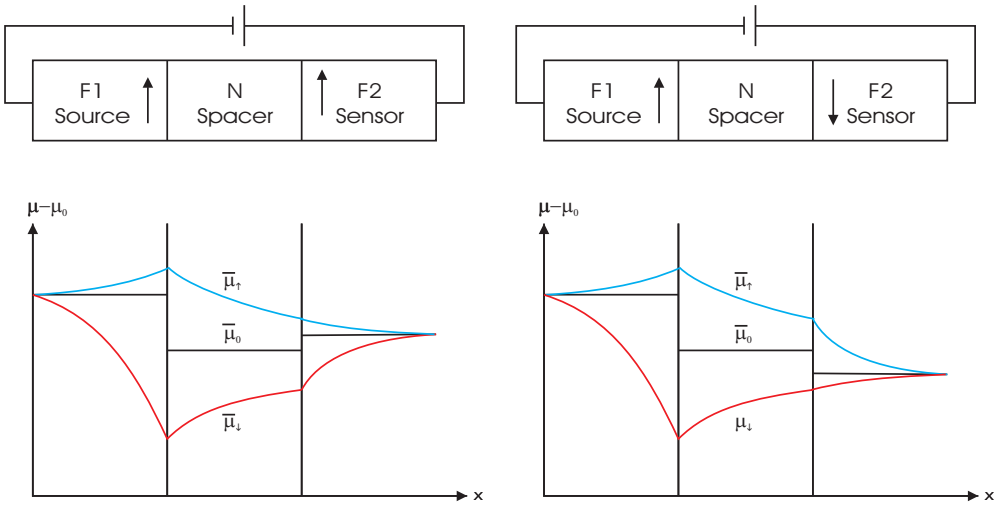

(a) Low resistance state (b) high resistance state

Figure 1.3: The electron chemical potential for the spin valve shown in figure 1.2. In the low resistance state, the spin accumulation voltages at the F1/N and N/F2 interfaces partially cancel, but in the high resistance state, the spin accumulation voltages add. Note that in this figure the average electric potential (μ_0) has been subtracted from the electrochemical potential ($\mu_{\uparrow\downarrow}$) to leave only the spin chemical potential ($\bar{\mu}_{\uparrow\downarrow}$).

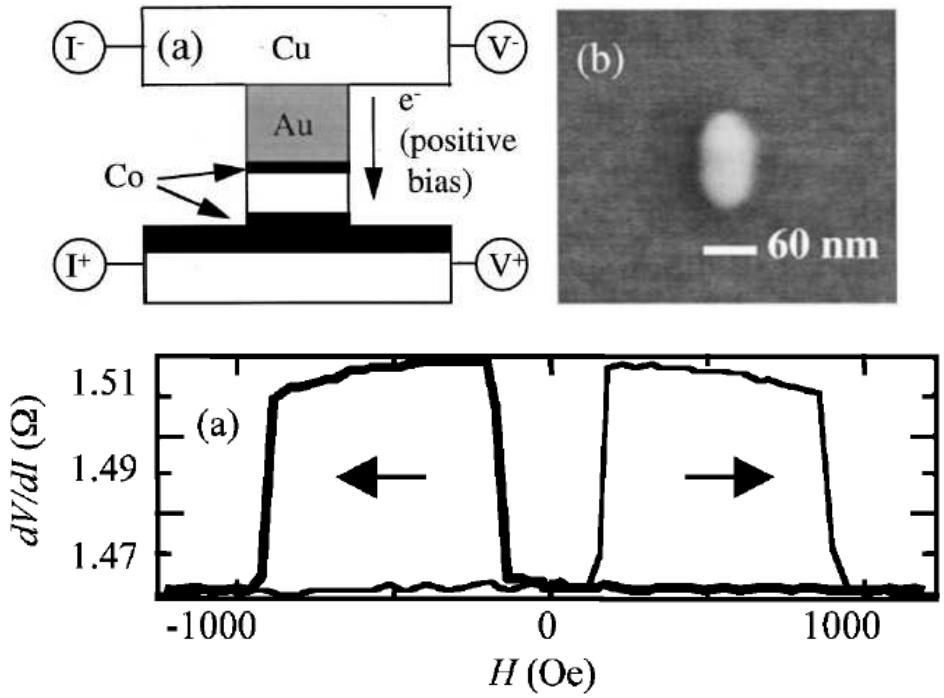

Figure 1.4: Albert *et al.* [2, 3] created a spin injection structure consisting of a magnetic multilayer buried within a pillar structure. The lowest graph shows a typical GMR curve for this type of structure. When the a large negative field is applied to the sample, both layers are aligned and the resistance is low. After the field is reversed, one layer switches in a small positive field and the resistance increases. In a large positive field, both layers become aligned again. The positive field to negative field sweep direction shows the same effect.

1.3 Spin-Transfer Torque

Using the GMR effect, a polarized current can be used to detect changes in the magnetic state of a sensor layer. However, if the polarized current is strong enough, it can alter the magnetic state of the sensor layer.

In a system as shown in figure 1.3, the reference ferromagnet polarizes the electrons, which then pass through the paramagnetic material. As the polarized electrons enter the second ferromagnet, two types of interactions occur. First, precessional motions in both the incident electrons and the ferromagnet, as shown in figure 1.5, are caused by non-equilibrium exchange interactions (NEXI) [38] between the injected electrons and the molecular field. However, the effective torque induced by NEXI interactions is nearly zero except for extremely thin samples of a few monolayers [39]. The effect is essentially canceled due to electrons in different k-states losing coherence to each other. Also, the electrons precess about the molecular field. Thus, after a short distance, usually about 1 nm, they have precessed 180°. This effectively cancels the torque from the electrons at the initial injection point.

Spin selective scattering will cause the second type of motion: damping. The average moment of the incident electrons will relax into the direction of the ferromagnet. Conservation of angular momentum requires that as the polarization of the incoming electrons is altered, their angular momentum must be absorbed by another part of the system. Although the angular momentum can be absorbed by the lattice, most is absorbed by the magnetic moment of the ferromagnetic material. Mathematically, this can be stated

$$\frac{\partial \vec{S}_1}{\partial t} = -\frac{\partial \vec{S}_2}{\partial t} \tag{1.6}$$

where $\vec{S}_1$ is the spin angular momentum per unit volume of the injected spins, and $\vec{S}_2$ is the spin angular momentum of the second ferromagnet. These values can be related to the polarization vector $\vec{P}$, which is the vector representing the expectation value of spin of the electrons, by $S = n\frac{\hbar}{2}\vec{P}$, where n is the spatial density of electrons.

This absorption effectively creates a negative damping: one in which the precessional cone can be opened from its equilibrium state. Slonczewski [26] and Berger

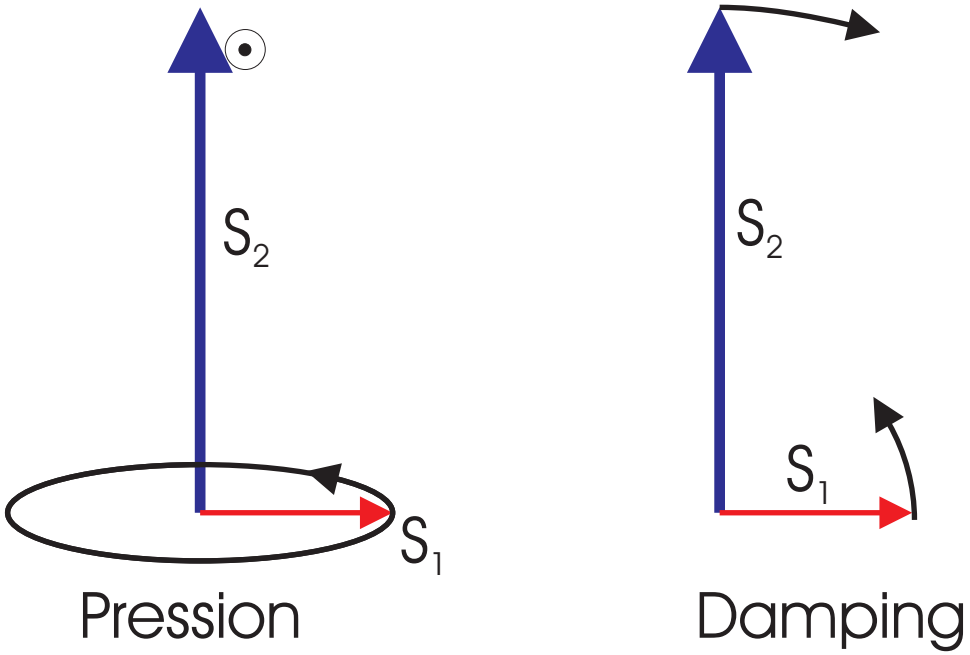

Figure 1.5: When electrons are injected into a ferromagnet, the magnetization is affected in two ways. The magnetic moment of the injected electrons (S_1) begins to precess about the exchange field of the ferromagnet (S_2). At the same time, S_2 precesses about S_1. However, since the moment of the ferromagnet is much larger than that of the incident electrons, the precession of S_2 is much slower than that of S_1. At the same time, spin dependent scattering causes the magnetic moment of the electrons to relax into the direction of the exchange field. Due to conservation of angular momentum, S_2 must also damp into the direction of S_1. Like the precessional case, the difference in magnitude of S_1 and S_2 causes the damping of S_2 to be much slower.

[27] found two similar equations. Berger's theory is based on considering spin wave excitations in a ferromagnet due to spin injection and gives an effective torque τ_d:

$$\tau_d = \alpha(\theta)(\Delta\mu + \hbar\omega)\frac{\vec{S}_2 \times \left(\vec{S}_1 \times \vec{S}_2\right)}{\hbar S_1 S_2^2} \tag{1.7}$$

$\alpha(\theta)$ is a dimensionless function that parallels the Gilbert damping parameter α in the Landau-Lifshitz-Gilbert equation. $\Delta\mu$ is the energy separation between spin-up and spin-down states. Note that this quantity is proportional to the injected current. Thus, the damping torque becomes stronger as the current is increased. ω term represents the precessional frequency of the lowest order spin-wave: coherent rotation.

By analyzing Berger's and Slonczewski's results for various configurations of S_1 and S_2, a very important qualitative difference between Oersted switching, i.e. using magnetic fields created by moving electrons, and switching by spin injection is found. Oersted switching is completely symmetric: by changing the current direction, the field reverses polarity and retains the same magnitude. Thus, the switching in each direction occurs at the same magnitude of current. However, spin injection is inherently asymmetric.

In most systems, one layer is fixed either due to exchange biasing or by changing the layer thickness to create a different coercivity. The sensor layer, which has the lower coercivity, is the only layer that switches. To obtain switching when the two layers are antiparallel, electrons pass from the fixed reference layer, through the non-magnetic layer, and into the second ferromagnetic layer as shown in figure 1.6. The reference layer serves as a spin polarizer. Although system dependent, for this argument, we will assume the emitted electrons are perfectly polarized along the majority direction of the reference layer. Upon entering the second ferromagnet, electrons with a minority polarization when resolved along the quantization axis of F_2, are reflected. The transverse component of the polarization vector represents angular momentum that is absorbed by F_2 due to spin selective scattering. This momentum is perpendicular to F_2 and causes a rotation into the direction of F_1, thereby aligning the two ferromagnetic layers.

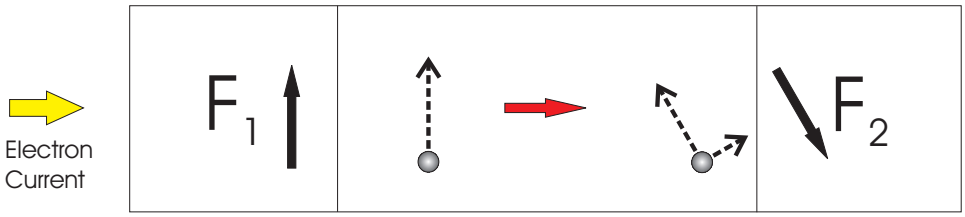

(a) Electrons are spin polarized by the reference layer F_1. The polarization vector can be decomposed into a longitudinal component along the quantization axis of F_2 and a transverse component.

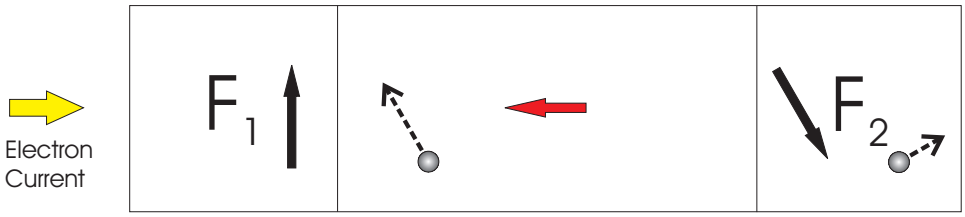

(b) Electrons with a spin polarization antiparallel to F_2 are then reflected while the transverse component of angular momentum is absorbed by the sensor layer due to spin dependent scattering. This transverse component is perpendicular F_2 and tends to align the two ferromagnetic layers.

Figure 1.6: When electrons pass directly from the reference layer F_1 to the sensor layer F_2, the transverse angular momentum is transferred to F_2 while the antiparallel component is reflected. The transferred angular momentum tends to align the two ferromagnets.

In the parallel configuration, the situation is a little more complicated as shown in figure 1.7. Polarized electrons exit the sensor layer and interact with the reference layer F_1. Again, spins with a polarization vector antiparallel to F_1 are reflected. As these electron encounter F_2, the transverse component of the angular momentum is again absorbed through spin dependent scattering while electrons with a polarization vector antiparallel to F_2 are reflected. The absorbed component of the angular momentum tends to align the ferromagnets antiparallel to each other.

The two cases are inherently asymmetric as the parallel to antiparallel switching case includes an extra reflection. This asymmetry can be measured from the difference in the critical currents between the two cases. Albert *et al.* [2] measured the critical currents necessary to switch the pillars shown in figure 1.4. Figure 1.8 shows a differential resistance vs. injected current for one such pillar. When strong negative currents are applied to the system, electrons flow from the fixed layer into the the

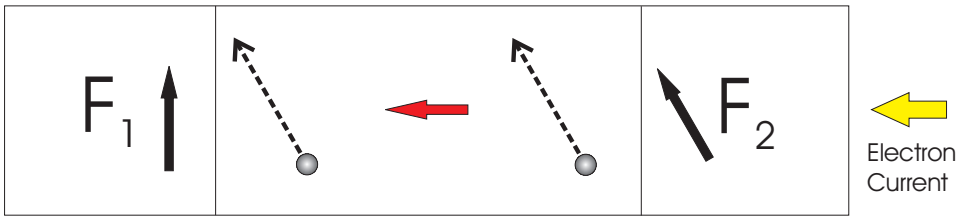

(a) Electrons are spin polarized by the sensor layer F_2.

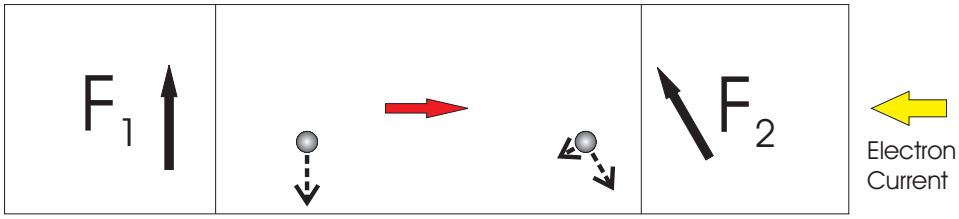

(b) Electrons with a polarization vector antiparallel to F_1 are reflected. As in the case of direct switching, the transverse component is absorbed into F_1. However, unlike F_2 in the previous case, the reference layer is pinned and the magnetic state cannot be altered so the momentum is absorbed by the lattice. The polarization vector of the reflected electrons can be decomposed into a longitudinal component along the quantization axis of F_2 and a transverse component.

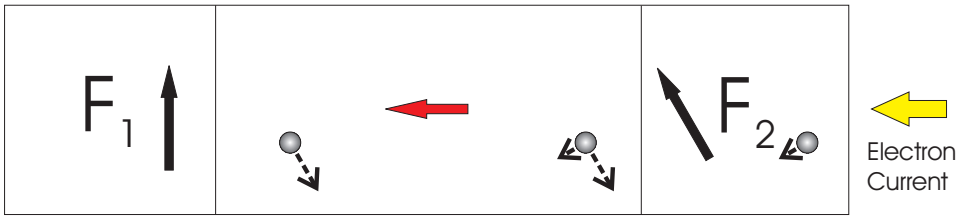

(c) Electrons with a spin polarization antiparallel to F_2 are then reflected while the transverse component of angular momentum is absorbed by the sensor layer due to spin dependent scattering. This transverse component tends to move F_2 antiparallel to F_1.

Figure 1.7: When electrons are injected from the sensor layer F_2 to the reference layer F_1, a series of reflections causes F_2 to become antiparallel to F_1.

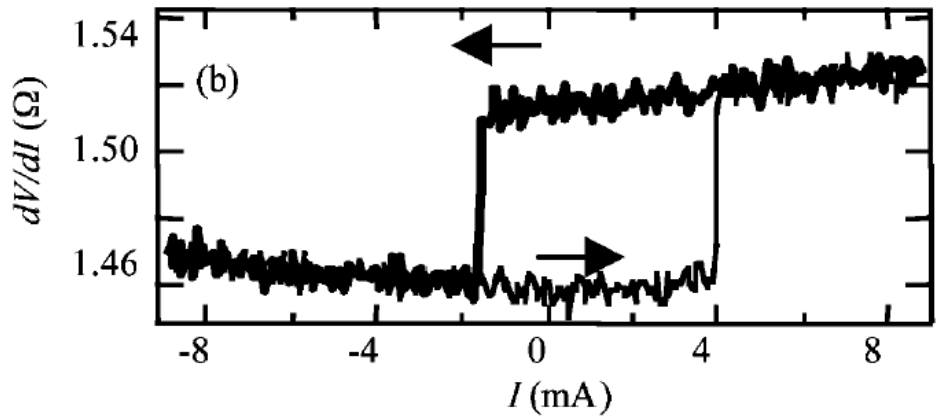

Figure 1.8: Electrical measurements [3] when current was passed through the structures shown in figure 1.4. The critical current necessary to cause a switching event is dependent on which direction the current flows. In the negative current direction, the spin polarized electrons travel directly from the polarizing reference layer to the sensor layer causing the two layers to align. In the positive current direction, the electrons are polarized by the sensor layer, reflected off the reference layer, and then interact again with the sensor layer to cause a switching event. The extra reflection needed for the positive current case produces an asymmetry in the critical switching current. This extra reflection results in efficiency losses, and thus more current is required. Further illustrations as to the causes of this asymmetry are shown in figures 1.6 and 1.7.

sensor layer. This favors a parallel configuration. As the current is swept to positive values, current flows from the sensor layer to the reference layer. The reflections favor the antiparallel state and the resistance becomes high. As the current is then swept back towards the negative polarity, electrons again flow from the fixed layer to the reference layer. This polarity favors the parallel configuration, and at a critical current the system switches to the low resistance state.

One other important practical consideration exists for negative damping to be a viable method of switching. Switching due to the Oersted field of the applied current is an alternate process. Conceivably, Oersted switching could be used to assist spin-injection switching. For example, when two ferromagnetic layers are perfectly antiparallel, there is no torque due to spin-injection. However, thermal motion will move one of the ferromagnetic layers out of this unstable equilibrium and a torque will begin. However, Oersted switching within a wire will also cause movement away from this

nonstable equilibrium and can assist the process. However, Oersted fields at opposite edges of a wire are in opposite directions. Thus, Oersted fields can favor a multi-domain state, which is often undesired. In order to balance these two effects for the best device, the size of the structure is crucial. Since Oersted fields are proportional to the current while spin-transfer torque is proportional to the current density, the structures must be small for uniform switching, usually on the order of 100 nm or less. Also, the magnetic switching layer must be thin since the spin-transfer torque occurs near the surface and decays rapidly in the bulk.

1.4 Summary

The possibility of using spin injection in magnetic applications looks very promising. Through a careful understanding of the chemical potential of each spin channel and the interfaces between ferromagnetic and normal metals, spin injection can be used to transfer spin information between two ferromagnetic layers. If the current density is sufficiently large, the bulk magnetic moment can be switched into a new stable state. Electrical measurements can be used to determine whether the source of switching is spin injection or Oersted switching by examining whether the magnitude of the critical switching depends on the current direction. However, direct imaging provides a more reliable, albeit much more difficult, method for observing spin injection.

Chapter 2

X-ray Measurement Techniques

Although much of the labor of this project was consumed in the sample preparation stages, the final goal of the project was to measure the magnetization state changes of these samples as a result of spin injection. This was accomplished using a photoemission electron microscope (PEEM) and a scanning transmission x-ray microscope (STXM). Both of these instruments can be used in various modes depending on what one wants to measure. Since magnetism was the main focus, the instruments were configured to take advantage of x-ray magnetic circular dichroism (XMCD), a powerful method that requires an energy-tunable source of circularly polarized x-rays.

2.1 X-ray Magnetic Circular Dichroism

Erskine and Stern were the first to propose x-ray magnetic circular dichroism in 1975 [40]. They calculated the core-to-valence resonance absorption spectra for circularly polarized radiation as a function of the magnetization in Ni. Their work would not be verified until 12 years later when Schütz *et al.* [41] used circularly polarized x-rays to examine absorption in iron. Thole *et al.* [42] and Carra *et al.* [43] then developed a more complete theory that would allow researchers to distinguish the signal of the spin and orbital magnetic moments from the total magnetic signal.

2.1.1 X-ray Absorption

To understand XMCD, one must first understand the basics of x-ray absorption. The famous Fermi's Golden Rule states that the probability of a photon absorption event between an initial state $|i\rangle$ and a final state $|f\rangle$ is

$$\frac{2\pi}{\hbar} |\langle f|D|i\rangle|^2 \delta (E_f - E_i - \hbar\omega) \tag{2.1}$$

where $\hbar$ is Planck's constant. E_f and E_i are the energy of the final and initial states, respectively. D represents the dipole operator, and ω is the angular frequency of the photon to be absorbed.

The first important aspect of this equation is the energy conservation requirement. The delta function requires that the energy change between the two electron states match that of the absorbed photon. Of course, in a band picture, there are a large number of final states, so for the true absorption probability, equation 2.1 must be integrated over all possible final states.

When the wavefunctions are known, equation 2.1 is sufficient for calculating the transition probabilities, at least to first order. However, even without knowing the wavefunctions, several more important insights can be found. First, the spin of the electron must be conserved. The dipole operator does not interact with the spin component of the electron, so the matrix element $|\langle f|D|i\rangle|$ will be zero unless the initial and final states have the same spin.

Secondly, angular momentum must be conserved. In XMCD the incident x-ray is circularly polarized and thus, carries $\pm\hbar$ of angular momentum. For convenience, a quantum number q can be defined that is 1 if the angular momentum of the incident light is $\hbar$ when measured along the quantization axis and is -1 if the angular momentum is $-\hbar$. In practice, instead of defining the angular momentum of the x-ray, the chirality is usually stated. Strictly speaking, this is not an important quantity because a right-handed circularly polarized (RCP) x-ray incident from above a sample has the opposite angular momentum as a RCP x-ray incident from below the sample even though the chirality is the same. However, given a particular equipment geometry, it is sufficient to know the chirality because the direction of incidence is

also known. Thus, for further discussion, I will assume the quantization axis to lie along the propagation vector of the x-ray, which results in a left-handed circularly polarized photon having a positive angular momentum. Upon absorption, this angular momentum must be transferred to the system. From these simple considerations, the following selection rules follow

$$\begin{aligned} \Delta\mathbf{S} &= 0 \\ \Delta\mathbf{L} &= \pm 1 \\ \Delta\mathbf{J} &= \pm 1 \\ \Delta m_j &= q \end{aligned} \tag{2.2}$$

From the above selection rules, several important facts arise. First, the subshell of the electron must change during the transition. For example, $p \rightarrow p$ transitions are not allowed. Although $p \rightarrow s$ transitions are allowed, this excitation channel is about 20 times weaker than the $p \rightarrow d$ transitions [44] and therefore, will not be considered in further discussions. Second, the angular momentum change of Δm_j must match the angular momentum of the incoming light. As will be described shortly, this underlies a disparity in the excitation probabilities of spin-up and spin-down electrons for a given polarization of light. Finally, $\Delta S = 0$ implies that there is no interaction between the incident light and the spin of the electron. Spin information can only be gained through spin-orbit coupling.

2.1.2 Sum Rules

In the form shown, the above selection rules tell which transitions can occur, but not the relative probabilities. XMCD takes advantage of the fact that given initial and final states, the transition probability depends on the angular momentum of the incident photons. The transition probabilities were derived by Stöhr and Wu [45]. For simplicity, we will consider a simple rigid band model. A more complete discussion of the merits and shortfalls of this model can be found elsewhere [46]. Also, a one-electron model will be used as opposed to a configuration model. While the configuration model is more complete and accounts for changes in all electrons

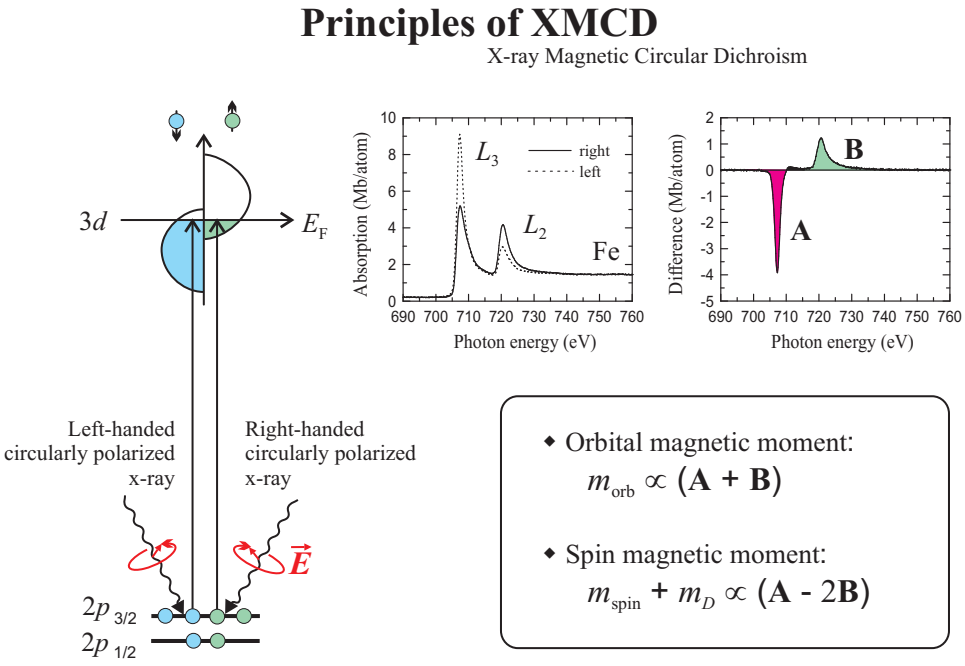

Figure 2.1: Spin-up and spin-down electrons have different transition probabilities when exposed to circularly polarized x-rays. Depending on the angular momentum of the incident photons, spin-down or spin-up transitions will be more probable. By comparing the spectra for each x-ray polarization, the orbital and spin moments can be determined. Unlike most other methods, these two quantities can be separated from each other when using XMCD. [4]

after a transition [45], it is more complex and is not necessary for this introductory discussion.

As shown in figure 2.1, the $3d$ state has an exchange splitting of the spin-up and spin-down sub-bands. In equilibrium, the electrons will attempt to fill the lowest energy states. Since the lowest energy states are spin-down, the electrons tend to preferentially occupy spin-down electronic states of the d-band. Recalling that the magnetic moment and the electron spin are in opposite directions, the entire material must have a magnetic moment in the up (or positive z) direction.

The $2p_{3/2}$ and $2p_{1/2}$ states are split due to spin orbit coupling. In one case the orbital and spin angular momenta add, and in the other they partially cancel. Although each of these two states have an equal population of spin-up and spin-down electrons, the two spin populations are not equally coupled to the orbital states. For example,

in the $2p_{3/2}$ state, the spin-up electrons are three times more likely than spin-down electrons to occupy p states with $m_l = 1$. However, the $2p_{3/2}$ state in total is occupied by two spin-up electrons and two spin-down electrons. This spin-orbit coupling causes the transition probabilities for a given x-ray polarity to be unequal. Assuming all d-states are unoccupied, when $q = 1$, the probability of exciting a spin-up electron is three times the chance of exciting a spin-down electron. The reverse is true when a negative polarization of light is used. Thus, the spin coupling of the $2p$ states is probed using circularly polarized x-rays. However, this yields little useful information because all the $2p$ states are occupied in the transition metals of interest. Positive and negative light polarizations can be used to excite more spin-up and spin-down electrons, respectively. However, an equal number of electrons in total will be excited by each polarity. In reality, the assumption that the d-states are unoccupied is incorrect for transition metals. If the spin-down channel is completely occupied while the other is completely unoccupied, the transition probability of the $2p_{3/2}$ state to the $3d$ state for a positive polarization will be reduced by 37.5% while the transition probability for a negative polarization will be reduced by 63.5%. Thus, by using two polarizations of light, the occupation, and thereby the moment, of the d-states can be probed.

Figure 2.1 shows a measured spectrum for the Fe L_3 and L_2 edges. When right-handed circularly polarized light ($q = -1$) is used, the L_3 peak is diminished while the L_2 peak is enhanced. The opposite is true for left-handed circularly polarized light ($q = 1$). By subtracting these two curves the difference spectrum can be calculated. By integrating the difference in area under the L_3 peak, area A, and the area under the L_2 peak, area B, the orbital and spin moments can be found by

$$\begin{aligned} m_{orb} &\propto A + B \\ m_{spin} + m_D &\propto A - 2B \end{aligned} \tag{2.3}$$

where m_{orb} and m_{spin} are the magnetic moments due to the orbital angular momentum and the spin angular momentum, respectively. XMCD is one of the few techniques that can separate these two terms. m_D is a spin density term and is related to the difference in the electron density in different directions within a unit

cell. Thus, unlike most other magnetic measurement techniques, m_D allows XMCD to measure direction dependent magnetization. If the angular average of $A - 2B$ is measured, the m_D term approaches zero and the bulk magnetization due to the spin can be found.

2.1.3 Examples of Methods Used in Image Acquisition

To obtain quantitative data for the magnetic moment, a full spectrum must be taken at each polarization. However, often qualitative information is sufficient. As will be explained in section 2.2, the scanning transmission x-ray microscope (STXM) and the photoemission electron microscope (PEEM) are both capable of taking XMCD images. Figure 2.2 shows how XMCD can be used to image the magnetic domains in Co. A single image taken at a resonance edge shows magnetic contrast. With spatial resolution, multiple domains are visible. Since opposing domains have different projections of their magnetization along the quantization axis of the x-ray, they will have different absorption intensities. As such, some domains will be darker than others. To enhance the contrast, an image can be taken at the L_3 and L_2 edges. These edges have opposite contrast. The regions that are dark in an L_3 image due to magnetic contrast will appear light in the L_2 image. These images are then combined and normalized, as will be described shortly, in order to enhance the magnetic contrast while suppressing the topographical contrast.

Although two areas with different magnetizations will have different absorption intensities, this is not the only contrast in an image. In fact, it tends to be one of the smallest sources of contrast. Topography often accounts for a much larger intensity fluctuation. Figure 2.3 shows an example where the the topographical contrast in the final image is much larger than the magnetic contrast.

Consider a sample that has three sources of absorption. First a background (B) absorption that accounts for uniform absorption across the entire image. Other forms of variation may also exist, such as topographical (ΔT) contrast. Finally, the desired contrast for XMCD images is the absorption differences due to magnetic variations (M). In practice $B \gg \Delta T \gg \Delta M$, which makes seeing the magnetic contrast

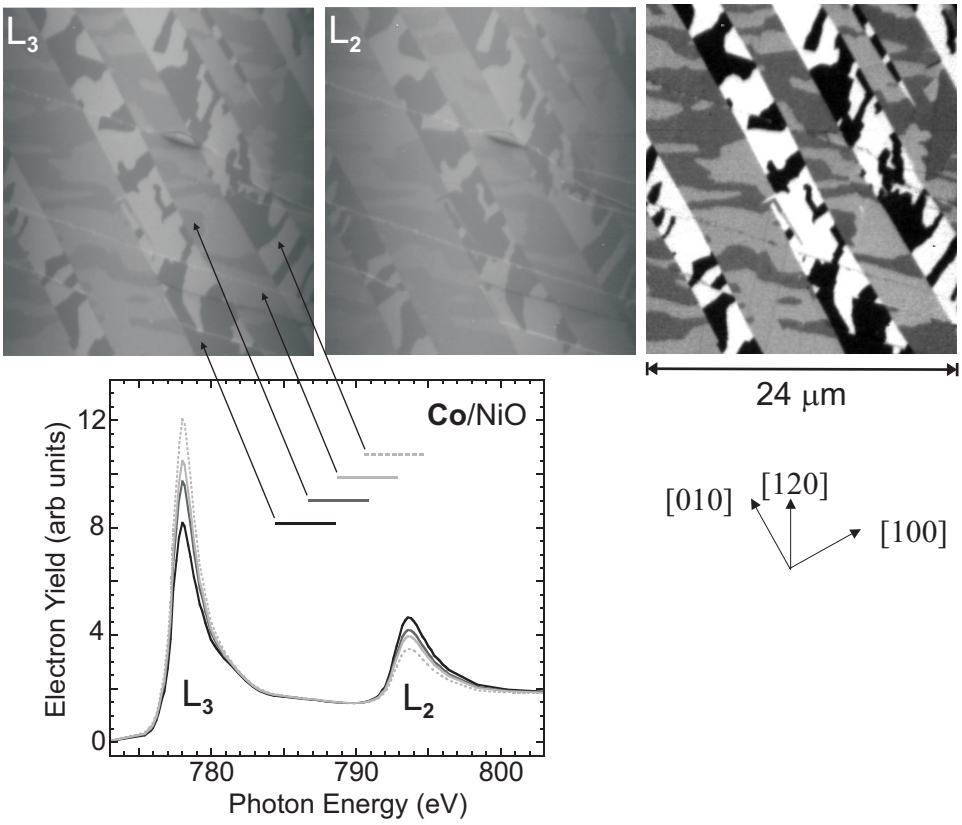

Figure 2.2: A magnetic contrast image, top right, is formed by dividing the images at the L_3 and L_2 edges. These two images have the opposite magnetic contrast but the same topographical contrast. For comparison, the full spectrum is shown for each type of domain. These PEEM images are of a Co film deposited on a single crystal of NiO. The orientation of the NiO crystal is indicated on the right of the spectra. [1]

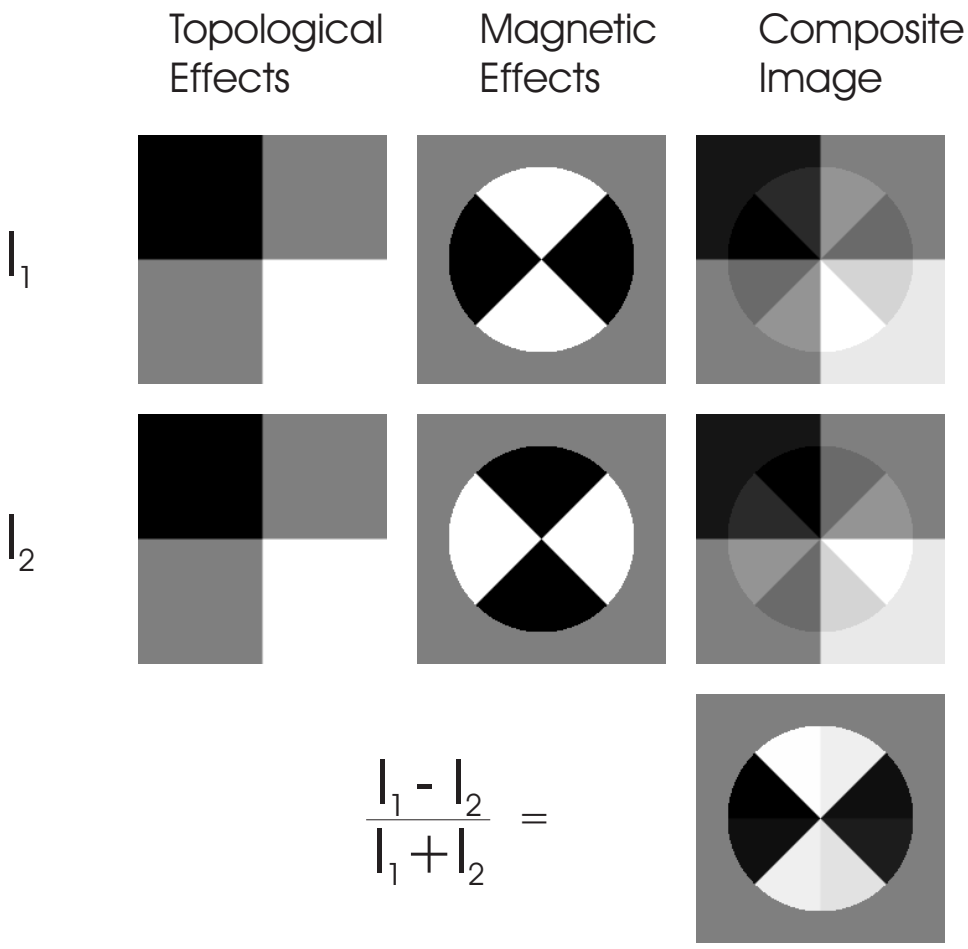

Figure 2.3: Two images are simulated that contain a constant background with topographical and magnetic contrast. When combined, the magnetic contrast is often much smaller then topographical or elemental contrasts. By subtracting and normalizing the images, the topographical signal can be suppressed while the magnetic contrast is enhanced.

directly very difficult. For example, in one data set used in the analysis in section 4.2.2, $\Delta T/B \approx 0.15$ while $\Delta M/B \approx 0.005$ These three types of absorption combine to form four regions:

$$\begin{aligned} &\text{Region 1} : B + \Delta T + \Delta M \\ &\text{Region 2} : B + \Delta T - \Delta M \\ &\text{Region 3} : B - \Delta T + \Delta M \\ &\text{Region 4} : B - \Delta T - \Delta M \end{aligned} \tag{2.4}$$

The smallest region of contrast is the difference in regions 1 and 2.

$$\text{contrast}_{1,2} = \frac{(B + \Delta T + \Delta M) - (B + \Delta T - \Delta M)}{(B + \Delta T + \Delta M) + (B + \Delta T - \Delta M)} = \frac{\Delta M}{B + \Delta T} \tag{2.5}$$

Since ΔM is very small compared to the other values, this contrast is exceptionally small, especially considering that regions 1 and 4 have a contrast of $(\Delta M + \Delta T)/B$, which can easily be an order of magnitude larger.

In order to enhance the magnetic contrast, two images (I_1 and I_2) need to be compared. In these two images, the magnetic contrast for each point must be inverted while all other contrasts remain the same. This can be done by inverting the polarization of the x-rays or taking images at two edges where the magnetization affects the absorption in opposite directions, such as the L_3 and L_2 edges as shown in figure 2.1.

If one then uses the transformation

$$I_M = \frac{I_1 - I_2}{I_1 + I_2} \approx \frac{I_1}{2I_2} - 1 \tag{2.6}$$

where I_1 and I_2 are the two images of reverse magnetic contrast, the four pixel intensities become

$$\begin{aligned} &\text{Region 1} : \tfrac{M}{B+\Delta T} \\ &\text{Region 2} : -\tfrac{M}{B+\Delta T} \\ &\text{Region 3} : \tfrac{M}{B-\Delta T} \\ &\text{Region 4} : -\tfrac{M}{B-\Delta T} \end{aligned} \tag{2.7}$$

Note that this method also allows sets of images to be compared because I_M is independent of the photon flux, which may vary with time in a synchrotron experiment. The approximation in equation 2.6 assumes that $I_1 \approx I_2$ at all pixels, which is almost always true because ΔM is so small. Also, in practice the images are simply divided since the -1 term and the 1/2 factor do not materially alter the image.

Using the transformation in equation 2.6 the minimum contrast of two pixels that have different magnetizations is $B/\Delta T$, while the maximum contrast from the topography that remains in the image is the inverse $\Delta T/B$. For the the values quoted above, this makes the signal-to-noise ratio greater than 40. Thus, using this method, the magnetic signal can be greatly enhanced while minimizing the other contrast mechanisms.

2.1.4 Summary

X-ray circular magnetic dichroism is a very powerful technique to determine the magnetization of a material. By taking spectra using two x-ray polarizations, the orbital and magnetic moments of a sample can be measured. If quantitative data is not needed, images can be taken at two transition edges that have opposite magnetic contrast mechanisms. By dividing these images, the magnetic contrast can be enhanced and the topographical contrast can be suppressed.

2.2 Instrumentation

In this work, two similar instruments were used: the scanning transmission x-ray microscope (STXM) and the photoemission electron microscope (PEEM). Each fits particular purposes best. The STXM is a transmission system, so the samples must be thin. The PEEM does not have this limitation, but its surface sensitivity makes it unsuitable for seeing buried layers. Although the STXM also tends to have better resolution, both are capable of producing high quality XMCD images.

2.2.1 Synchrotron Radiation

Both the STXM and PEEM use x-rays produced from a synchrotron. For XMCD to be effective, the energy of the x-rays must be tunable. As such, laboratory sources are not well suited for these types of instruments. The PEEM used in this project had a bending magnet source. As shown in figure 2.4, a strong permanent magnet deflects electrons along a curved path. The electrons, which are traveling near the speed of light, emit a cone of radiation that can then be harnessed for XMCD experiments. The x-ray polarization is chosen by selecting a section of the cone either above or below the rotation plane of the electrons. The STXM uses an undulator source, also shown in figure 2.4. In this system, a series of alternating permanent magnets causes the electron to be deflected in an oscillatory path. As the electrons are deflected, x-rays are emitted. Undulators are generally produce a higher flux of x-rays, and in some undulators the x-ray chirality can be chosen by altering the phase of the top and bottom sets of magnets.

Within the synchrotron, the electrons are not equally spaced. By using an RF electric field, the electrons are separated into a series of bunches. As each bunch passes the beam line, it emits an x-ray pulse. At the Advanced Light Source at the Lawrence Berkeley National Laboratory where these experiments were done, the x-ray pulses were separated by 333 ns.

2.2.2 STXM

The scanning transmission x-ray microscope (STXM) is a powerful instrument for imaging the magnetic and chemical structure of materials. Unlike many other instruments, the STXM can operate in a wide variety of environments [47, 48, 49] and does not require vacuum. As shown in figure 2.5, the basic operation involves taking a monochromatic x-ray beam and focusing it using a zone plate. Because the energy of the incident x-rays must match the absorption edge of the species of interest, the source must be tunable. Hence, a synchrotron is used as the light source. Since the zone plate produces multiple orders of diffraction, an aperture is needed to select the desired beam as shown in figure 2.6. After passing through the sample, the photon

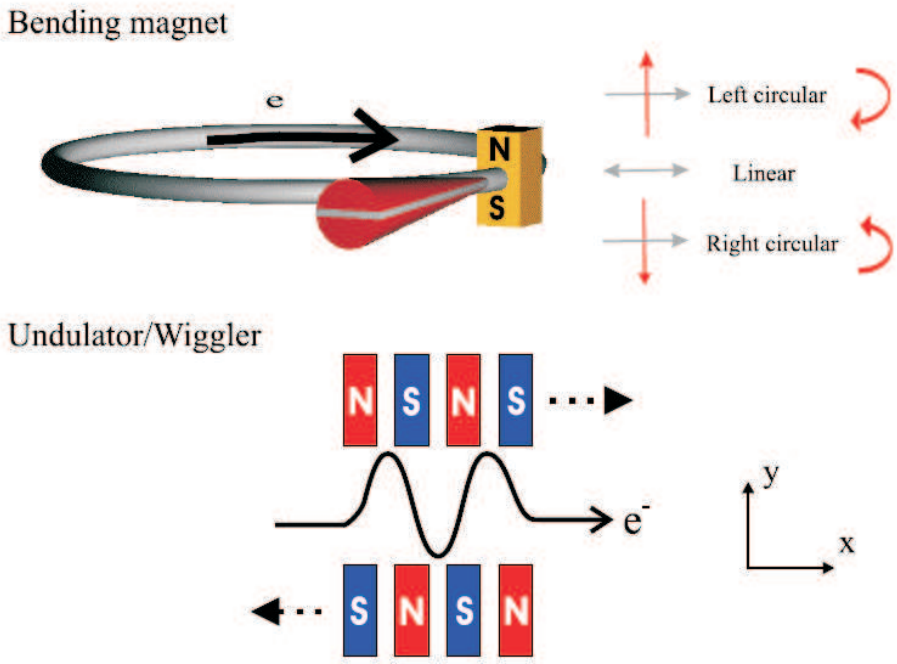

Figure 2.4: A bending magnet and an undulator can both be used to create x-rays from a synchrotron. The bending magnet (yellow) deflects electrons along a curved path. The electrons then emit x-rays that can be used in the STXM and PEEM for XMCD experiments. An undulator works in a similar way except that a series of alternating magnets are placed near the electron path. The magnetic fields from the magnets cause the electrons to be deflected in an oscillatory path that also causes the electrons to emit x-rays. [5]

flux is measured using a photodiode. Although the STXM is extremely simple in theory, several practical considerations exist that complicate the actual experimental technique.

Since conventional mirrors are ineffective at focusing x-rays, a zone plate must be used to focus. For a zone plate with an outermost zone of width $\triangle r$, the theoretical Raleigh resolution is $0.9\triangle r$ to $1.22\triangle r$, depending on the size of the central stop relative to $\triangle r$ [50]. However, the actual resolution is slightly less due to the fact that a finite source illuminates the zone plate [51]. Further details of the applicable optics for STXM can be found elsewhere [52].

Since STXM is a scanning technique, precise control of the sample position is crucial. For maximum control, the stage often has a course stage for large motions with a piezoelectric stage mounted on top for the fine controls. Thermal instabilities can cause drift in the course stages, so these are usually deactivated during the most precise measurements. Also, the system used in this work was filled with 20 mTorr of He to allow better heat dissipation than vacuum while having less absorption than air. Scanning is done using piezoelectric stages with a interferometer to precisely determine the position. The entire system is located on a polymer granite slab that damps low frequency vibrations. A system of support struts maintains mechanical rigidity of the system.

To detect the x-rays transmitted through the sample, a granular phosphor is deposited via sedimentation on the tip of a lucite rod. After being converted from x-rays into visible light by the phosphor, the light travels down a lucite pipe and is detected on a photomultiplier tube. For a more complete description of the experimental setup used at beamline 11.0 of the Advanced Light Source of the Lawrence Berkeley National Lab, Berkeley, CA, see [53]. Note that the STXM described in this reference refers to beamline 7.0, but this STXM was moved to beamline 11.0 before commencing this work.

Specialized electronics

For the experiments described, the normal electronics were altered significantly to allow for time-resolved measurements. Two aspects of the electronics were altered:

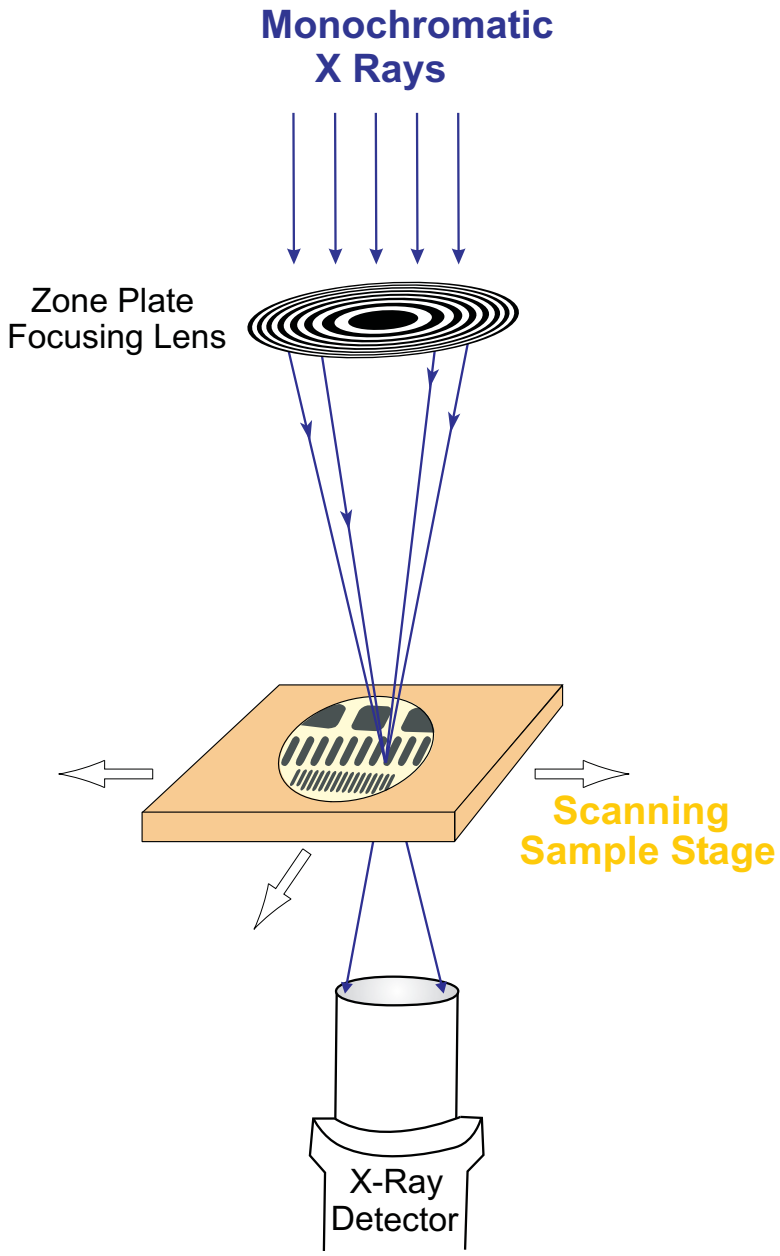

Figure 2.5: In a STXM, a zone plate is used to focus x-rays on a single point of the sample. A photodiode is used to measure the x-rays that are transmitted through the sample. The sample is then rastered to form a complete image of the sample. STXM is compatible with a wide range of x-ray techniques including XMCD. [6]

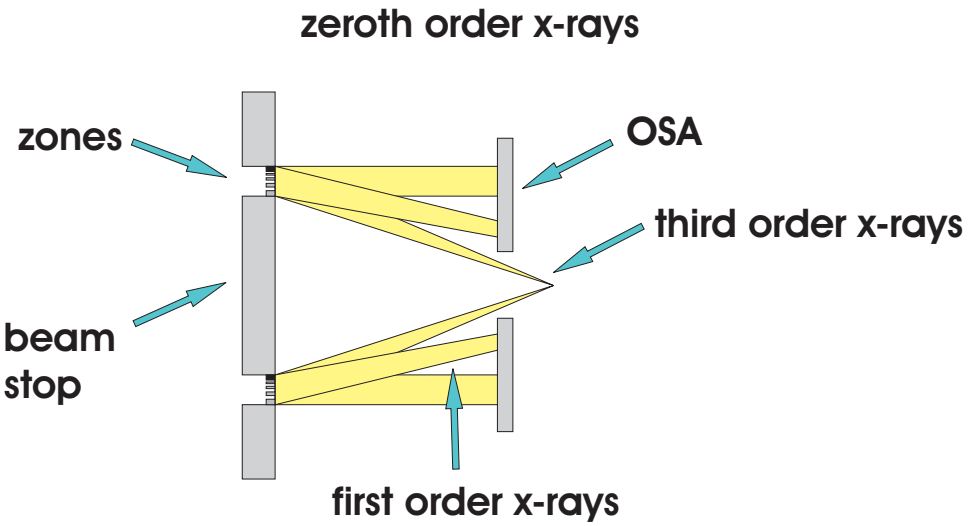

Figure 2.6: An order selecting aperture (OSA) is necessary to choose a single diffraction order of the zone plate.

the signal analysis system was rewired, and a pulsing source was added.

Figure 2.7 shows the pump-probe method used. During these measurements, the STXM was operating in two-bunch mode, which signifies that only two electron bunches exist in the synchrotron ring at any given time. In this mode, the synchrotron operates at 3 MHz, so the x-ray pulses are separated by 333 ns. First an electrical excitation pulse of 12-15 ns passes through the sample. This serves to disturb the magnetization and create a non-equilibrium state. After a short delay, x-rays arrive at the sample to probe the magnetic state. This pulse is considered the "hot" x-ray pulse because it measures a hot or excited state of the system. After approximately 100 ns following the start of the excitation pulse, an electrical reset pulse of 20 ns arrives in order to return the system to the original state. This pulse is only significant if the system were to fully switch from one stable configuration into another by the initial excitation pulse. In this case, the reset pulse would reverse the sample back to the first state. Finally, a second x-ray pulse arrives and probes the sample a second time. This is the "cold" x-ray pulse and serves to determine the relaxed state of the system. These two images are then used to determine the difference between the excited and reset state. By taking the images at nearly the same time any intensity fluctuations in the x-ray source can be eliminated when the images are divided. This

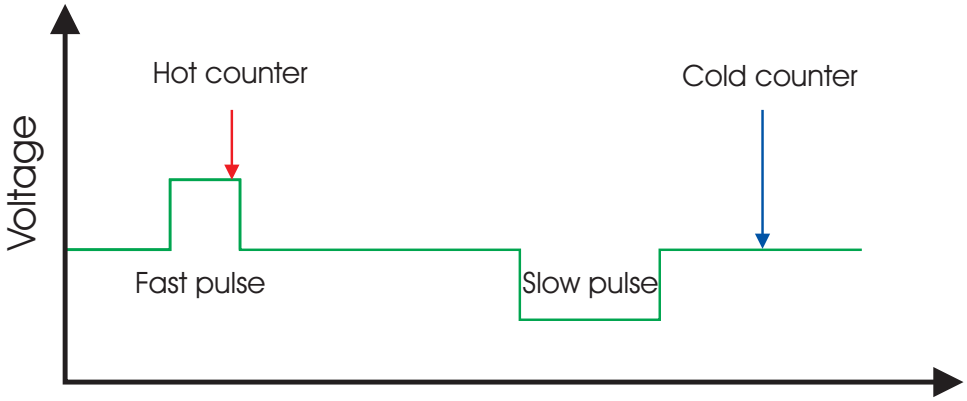

Figure 2.7: The samples were electrically pulsed for 12-15 ns. During the current pulse, an x-ray pulse comes and probes the magnetic state of the sample. A second pulse of the opposite sign then resets the sample to the original state. This pulse is only necessary if the sample's magnetic state were irreversibly changed, i.e. switched to another stable state. The image is then probed again with a second x-ray pulse. These two probing steps are sent to different counters and the process is repeated many times in order to obtain a good signal-to-noise ratio.

entire process is then repeated to build up good statistics at each data point on the sample.

The initial photon detection was made using a photomultiplier tube mounted behind the sample in the STXM. The signal was amplified and sent to a comparator to determine if a photon had truly been detected. A binary signal was then sent to a field programmable gate array (FPGA) which determined whether the measurement was on a hot or cold bunch. The signal passed to the appropriate counter which totaled the number of detected photons for either the hot or cold state. After the measurement of a pixel, the total count was sent to a computer, and the counters were reset.

One extra consideration was necessary when designing this system. First, the two bunches could have different intensities. As such, this difference would appear in the hot versus cold signals but would not indicate a true difference in the magnetic states. To solve this problem, the electrical pulse train was shifted by one x-ray pulse every 255 cycles. This shifting exchanged which bunch was being used to measure the excited and ground states and effectively eliminated the effect of any intensity

difference between the two bunches.

STXM is an extremely powerful technique for measuring magnetic information within a sample. It is sensitive to bulk properties and requires a thin sample for transmission. However, it also provides an unparalleled resolution with elemental specificity. With a few modifications to the electronics, the STXM can be used for time resolved experiments that show how the magnetization of a sample evolves as it is excited with electrical pulses.

2.2.3 PEEM

Unlike the STXM, the photoemission electron microscope PEEM is a surface sensitive technique that uses secondary electrons to image a sample. This work used the PEEM-2 apparatus at the Advanced Light Source in the Lawrence Berkeley National Laboratory, Berkeley, CA. A full description of this system can be found in Anders *et al.* [54]. Here, I will provide a brief discussion of the system and underlying concepts.

As shown in the schematic in figure 2.8 monochromatic x-rays are focused on a sample. However, unlike the STXM, the ultimate resolution has little to do with the degree of focusing. Ideally, the entire area being imaged should be uniformly illuminated. All points on the surface will absorb the x-rays and create excited electrons. However, if the absorption coefficient varies laterally across the surface, the electron yield will also vary. The excited electrons that escape from the surface are then passed through a series of electrostatic lenses that act to magnify the image onto a CCD camera. Within the electron path, an aperture exists in the back focal plane to select the low-energy secondary electrons.

2.2.4 Summary

Both the STXM and PEEM are extremely powerful techniques. The choice of which instrument to use depends on the sample requirements. Specifically, the STXM has higher resolution and requires thin samples. The latter requirement makes sample preparation significantly more difficult. Alternatively, the PEEM is surface sensitive. For certain samples this is highly desirable, but for the stencil and subtractive samples

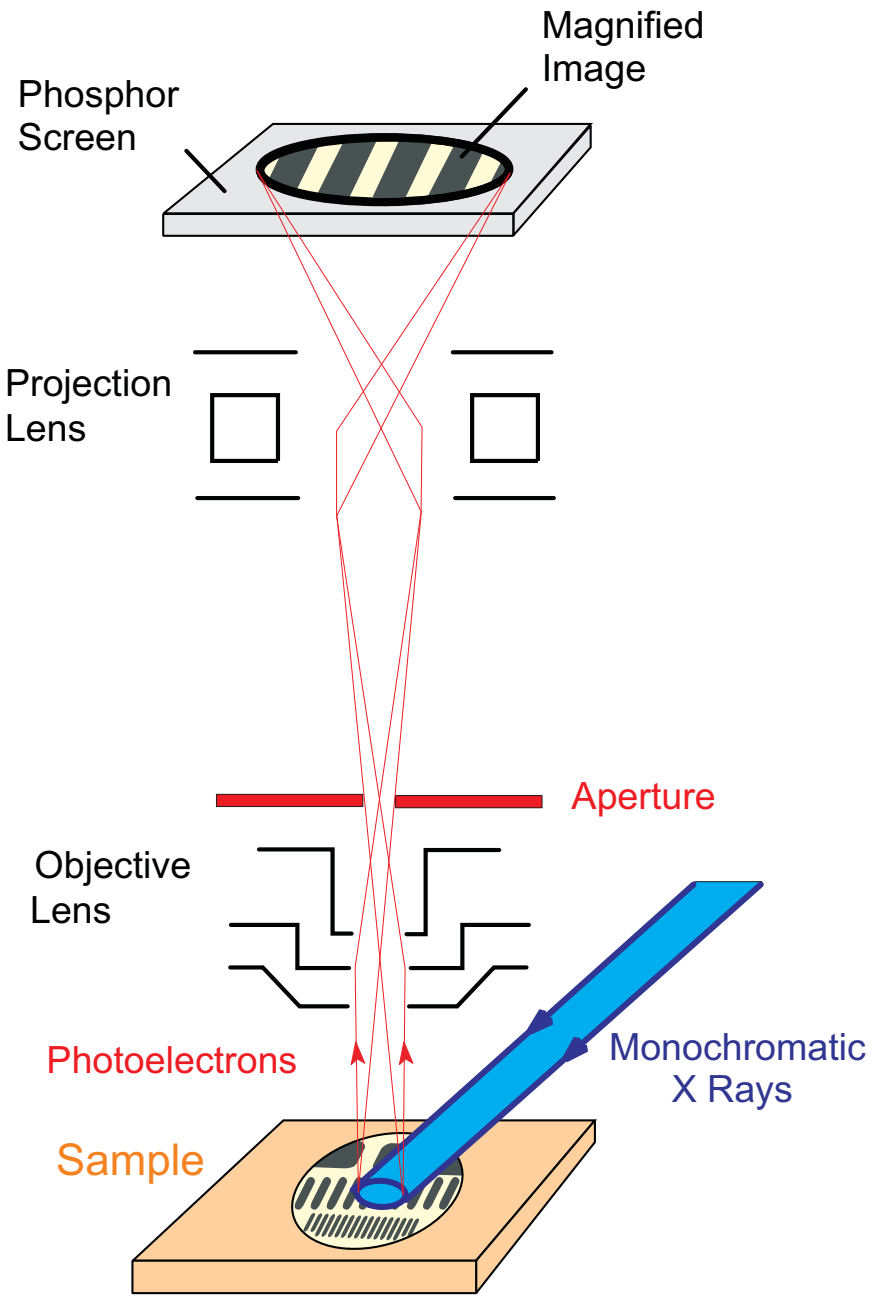

Figure 2.8: The PEEM illuminates an area of the sample with polarized x-rays. These x-rays excite secondary electrons in the sample. Electron optics are then used to gather the electrons that escape the sample and to reconstruct an image of where the electrons originated. Depending on the mode used for the measurement, an elemental, chemical, or magnetic image of the sample can be constructed. [6]

to be discussed later, the layers of interest are buried, so the PEEM is not a suitable choice. Magnetically, both work via XMCD. However, the x-ray sources of the two instruments at the Advanced Light Source are different. The STXM uses an undulator which has much better control of the x-ray polarization than the bending magnet used at the PEEM beam line. Both instruments have proved invaluable to the advancement in the understanding of magnetic phenomena.

Chapter 3

Membranes

Although the first set of experiments conducted were intended to be the simplest, interpreting the results proved extremely difficult. Initially, lithographically patterned samples were thought to require a long and complicated process since many steps would be necessary to complete the final structures. Eventually, this type of sample was necessary and required much effort, but initial work was done with a more novel approach which involved using a focused ion beam (FIB) to create small holes in silicon nitride membranes which could then be filled with magnetic materials.

As described previously, to see spin injection the current density in a sample must be extremely high. At the same time, the total current cannot become excessive or heating will destroy the sample. In order to achieve these two goals, first small holes were drilled into silicon nitride membranes. Multiple holes were drilled in close proximity to allow the region influenced by the spin injected current to be sufficiently large for imaging in the PEEM while still keeping the total current relatively low. The samples were then filled with magnetic and nonmagnetic metals to form a spin sensitive structure. Importantly, the metals must be deposited from both sides in this configuration. One set of samples had the magnetic reference layer deposited from the backside. The spacer and magnetic sensor layers were then deposited from the topside. In the other sample configuration, the backside was filled with a nonmagnetic metal, and the entire spin sensitive structure was deposited from the topside.

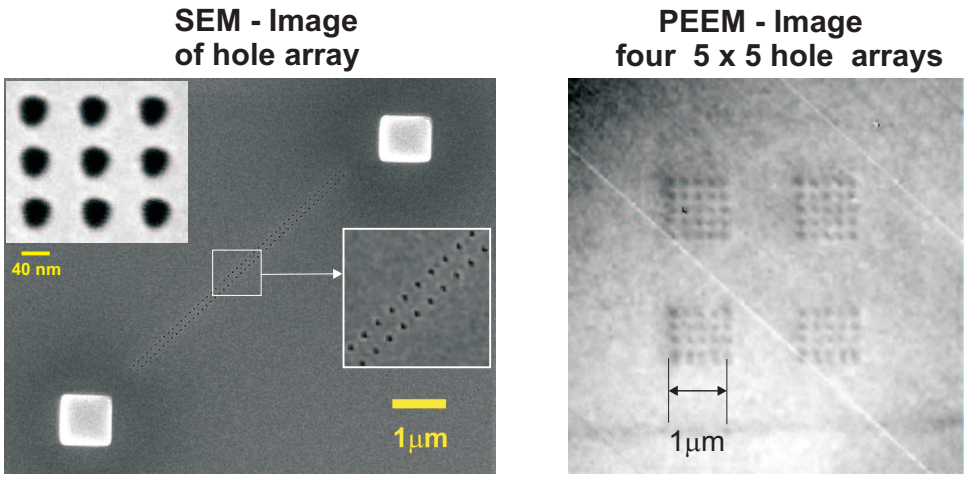

Figure 3.1: SEM and PEEM images of holes drilled by FIB into a low-stress silicon nitride membrane

For all samples, pre-fabricated membranes were purchased from an outside manufacturer (Silson, Ltd.). The low-stress silicon nitride measured 30 nm thick and $75 \times 75\mu m^2$ in the lateral dimensions. The membranes were suspended on silicon frames that were 200 μm thick and 10 mm in the lateral dimensions. Initially windows of $150 \times 150\mu m^2$ per side were used, but these proved to be too fragile and routinely broke due to electrical discharges when measured in the PEEM.

For all samples, the first step was for Dr. Charles Rettner at IBM to drill holes in the silicon nitride. The holes ranged in size from 30 nm to 60 nm. SEM and PEEM images of the drilled holes are shown in figure 3.1

3.1 Magnetic Backside

The first set of samples was produced as shown in figure 3.2. FIB was used to drill holes on the order of 40 nm into the silicon nitride membranes. The entire sample was then taken to a dc magnetron sputter deposition chamber located at IBM. Copper was deposited from the front side in order to predominantly fill the holes. The sample was then flipped over and a magnetic reference layer of either pure Co or $Co_{.90}Cr_{.10}$ was deposited on the back side. Although this two-step process was intended to minimize the topological effects of the holes on the magnetic structure of the Co or $Co_{.90}Cr_{.10}$,

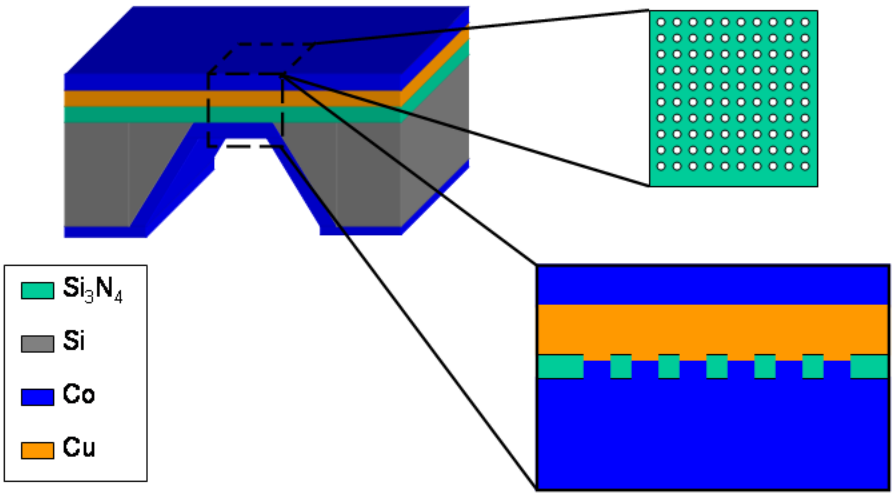

Figure 3.2: Schematic of sample preparation for backside membrane samples. After holes were drilled into a silicon nitride membrane, they were filled with copper from the topside. Next a magnetic reference layer was deposited on the backside. Vacuum was broken, and the sample was transported to the PEEM. There, after briefly sputtering the Cu to clean the surface, the thin sensor layer was deposited on the topside of the sample in-situ

the magnetic state near the hole could never be confirmed due to its small size and buried location.

The samples were then transported to the PEEM (see section 2.2.3) at the Advanced Light Source. After magnetizing the lower layer longitudinally in a 1 kOe field and a brief sputtering of the top Cu for cleaning, a magnetic sensor layer of Fe, Fe_xNi_{1-x}, or Co was then evaporated onto the sample. In an attempt to ensure that the magnetic state of the reference layer was fixed, it was made significantly thicker than the topmost sensor layer: 100 to 160 nm thick as opposed to 2 to 3 nm thick.

The results of these samples left much to be desired. After overcoming the problem with the membrane being too large and fragile, came the problem of how to

characterize the magnetic character of the samples. Due to the surface sensitivity of the PEEM, only the top layer could be magnetically imaged. The backside area of interest was deep within the cavity formed by the etched silicon. This depth of 200 μm created too much stray electric field for the PEEM to operate effectively. Thus, limited information could be obtained about the reference layer with the equipment available at the time.

Figure 3.3 shows the changes in the magnetic structure as various magnetic fields are applied. For this specific sample, the backside had 100 nm of $Co_{.90}Cr_{.10}$ deposited, while the topside had 50 nm of Cu. Vacuum was broken, and the sample was transported to the PEEM. After applying a 1 kOe field, the sample was sputtered to clean the Cu. Finally, 30 Å of $Fe_{.60}Ni_{.40}$ was evaporated onto the topside of the sample. In each picture, the membrane corner is clearly visible and has a different magnetic character than the permalloy not on the membrane. Although 1 kOe should easily set such a thin $Fe_{.60}Ni_{.40}$ layer, the field did not entirely magnetize the structure. This raised concerns that something about the membrane was affecting the $Fe_{.60}Ni_{.40}$ in an unforseen way.

In another sample (backside: 100 nm $Co_{.90}Cr_{.10}$. frontside: 50 nm Cu / 2.7 nm $Fe_{.20}Ni_{.80}$) the magnetic structure was imaged in both the normal configuration and at 90 degrees. This allowed a more complete understanding of the magnetization as shown in figure 3.4

Experiments were conducted by applying various combinations of positive and negative current through the samples, but no clear signs of spin injection were seen.

3.2 Magnetic Frontside

Although not completely proven, the difference in the magnetic structure as seen on the membranes and away from the membrane was probably due to stray fields of the lower layer. Since the lower layer was also deposited on the walls of the etched silicon underlying the membrane window, the magnetic structure of the lower fixed layer near the edge of the window probably had out-of-plane components. These components would be expected to create stray fields and possibly influence the magnetic state

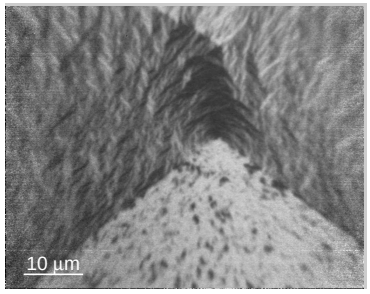

(a) As grown.

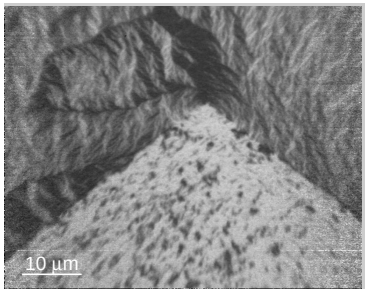

(b) 25 Oe applied perpendicular to the underlying $Co_{.90}Cr_{.10}$.

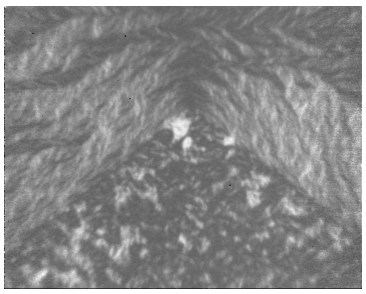

(c) 150 Oe applied perpendicular to the underlying $Co_{.90}Cr_{.10}$.

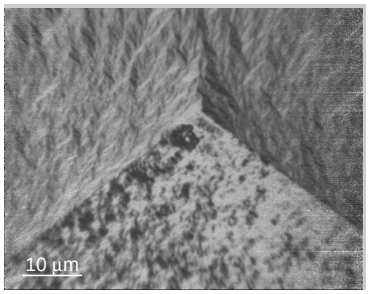

(d) 113 Oe applied antiparallel to the underlying $Co_{.90}Cr_{.10}$.

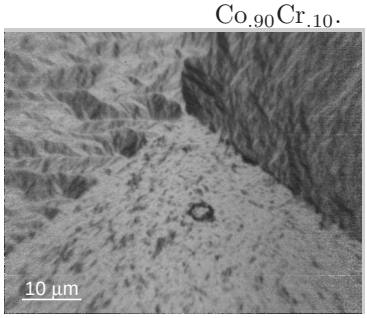

(e) 1 kOe applied parallel to the underlying $Co_{.90}Cr_{.10}$.

Figure 3.3: Progression of magnetic state as various fields were applied in succession. Under none of the conditions tested could the magnetic film be uniformly magnetized. All images readily show the corner of the underlying window etched into the Si wafer. This is probably due to stray fields from the Co or $Co_{.90}Cr_{.10}$ deposited on the walls of the window etched into the Si wafer. Unlike the holes imaged in figure 3.1, the holes are not visible because metals have been deposited before imaging.

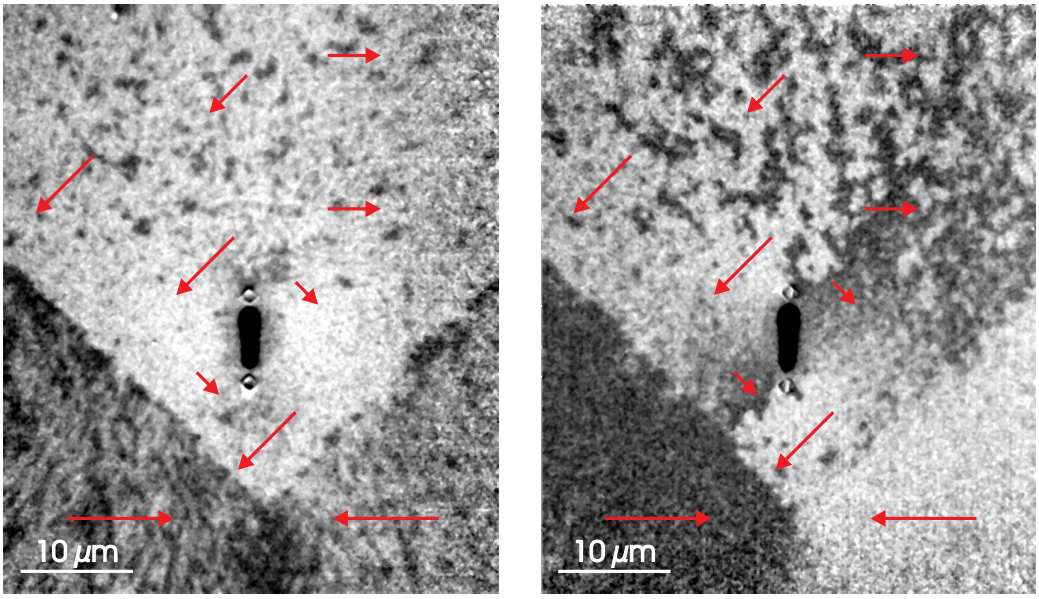

(a) Axis of measurement is vertical (white: up, black: down)

(b) Axis of measurement is horizontal (white: left, black: right)

Figure 3.4: The magnetic structure outside the membrane was highly influenced by the edge of the membrane. The magnetic materials on the membrane were non-uniformly magnetized. The black oval is a tear in the membrane where the holes were drilled. Although the tear prevented meaningful measurements for spin injection on this sample, it should not significantly affect measurements on the magnetic structure of the membrane as a whole when magnetized by external fields. Small Pt markers can be seen above and below the tear. These were deposited using FIB so that the holes could be located in the PEEM.

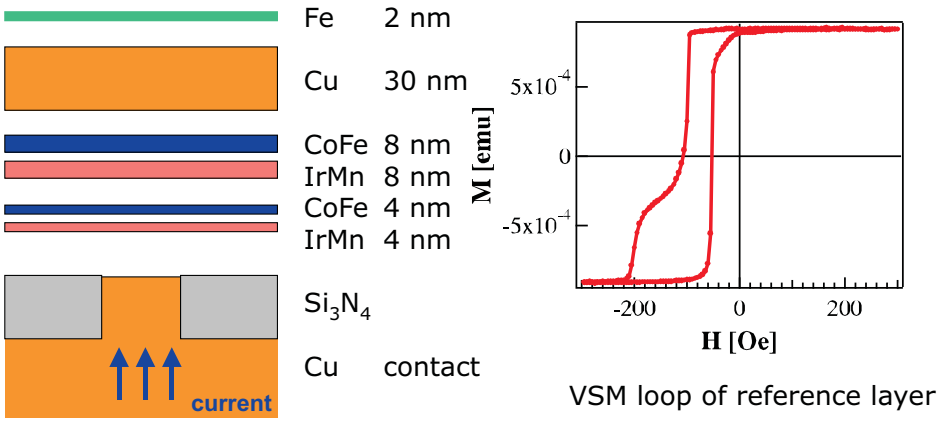

Figure 3.5: Left: Schematic of topside membrane structures. In this configuration, all magnetic layers were deposited on the top of the samples. The reference layer was composed of two exchange biased layers. Right: As shown in this VSM loop of the reference magnetic bilayer, the magnetic state was independent of the prior magnetic history.

of the membrane over the window. In order to eliminate this problem, all magnetic layers were then deposited on the top of the window. The bottom lead through the holes were filled with Cu prior to the topside deposition. After several inconclusive results, new samples were created with the reference magnetic layer exchange biased as shown in figure 3.5. A VSM loop of the reference layer is also shown. The nice feature of this setup is that under zero applied field, the magnetic state is the same regardless of the previously applied field.

As in the backside membrane case, switching was observed near the holes as shown in figure 3.6. However, the results were again inconclusive. Initially, a single domain appeared at 60 mA of current. However, it was in a localized area and not along the entire line of holes as would be expected. Also, at increasing currents, the Oersted switching was significant and could not be easily separated from any spin injection that might exist. As shown in figure 3.7, switching can be seen far from the area of the holes. With switching at distances well beyond 10 μm, the effects observed cannot be solely attributed to spin injection.

Due to the inconclusive nature of these results, the membrane structures were replaced by a new stencil structure that proved much more difficult to fabricate but

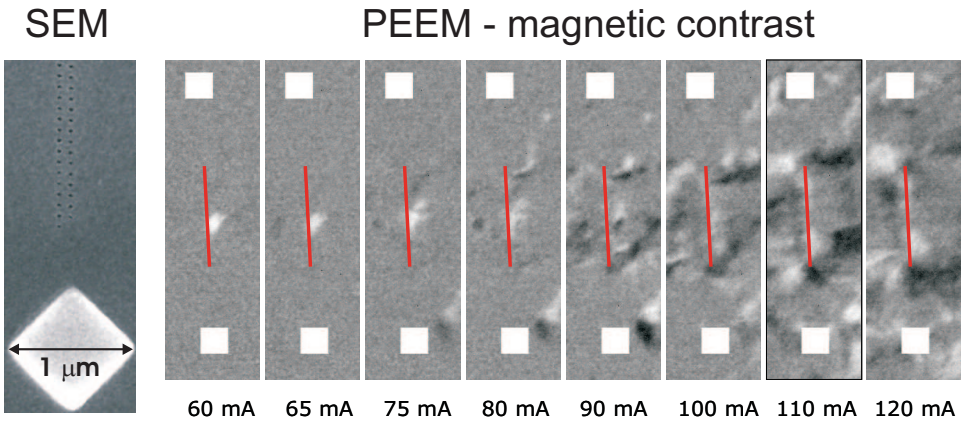

Figure 3.6: Left: SEM image of holes in Si_3N_4 membrane. Right: PEEM images showing magnetic contrast as a function of current sent through the sample. Dark and white areas correspond to switched domains whose magnetization are pointing down and up, respectively. The red line, which is 5 μm long, indicates the position of the holes, which are not readily visible by PEEM once metal has been deposited.

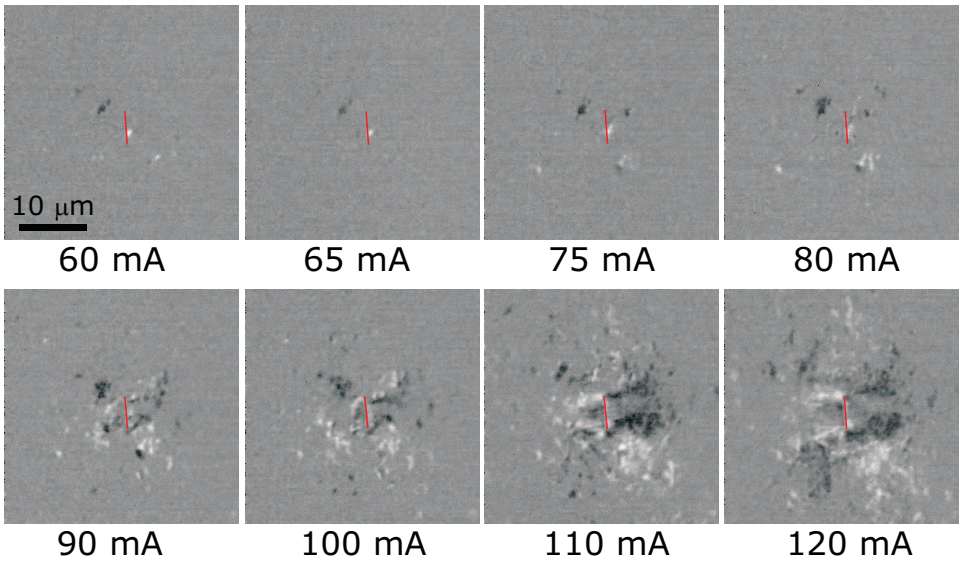

Figure 3.7: Magnetic domains formed over large regions as current was passed through the structure. The red line corresponds to the 5 μm double line of holes. The large areal distribution cannot be explained by spin injection alone. Oersted fields were clearly contributing to the observed switching pattern.

much easier to analyze.

Chapter 4

Lithographically Patterned Samples

After deciding the membrane samples were not viable to fully understand spin injection, a new process was designed. This new method involved significantly more complexity during the fabrication.

4.1 Stencil Samples

4.1.1 Processing

Although several samples that will be discussed vary slightly, they all share a basic fabrication process. For details about each piece of equipment, see appendices A.1 and A.2. The processing parameters are detailed in appendix B. Figure 4.1 shows the stencil sample at various stages in the processing line. Although this was the final version of the processing sequence, several samples that will be discussed had minor variations to this sequence.

The samples started from a double-sided polished wafer with 200 nm of low-stress Si_3N_4 deposited on each side using chemical vapor deposition (CVD) in the tylan nitride furnace. The nitride was necessary to later create a free standing membrane for x-ray transmission experiments. In general Si_3N_4 deposited by chemical vapor

(a) After 2000 Å of Si_3N_4 were thermally deposited on a double-sided Si_3N_4, 100 nm of Pt is sputter deposited and patterned by lift-off.

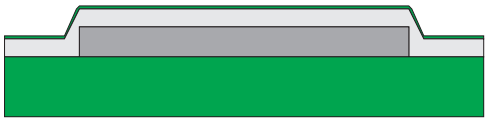

(b) 60 nm of SiO_2 and 10 nm of Si_3N_4 were deposited using PECVD.

(c) PMMA was spun and patterned using e-beam lithography. The Si_3N_4 was then etched to be used as a mask.

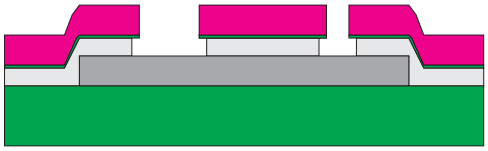

(d) The SiO_2 was etched in HF to form an undercut.

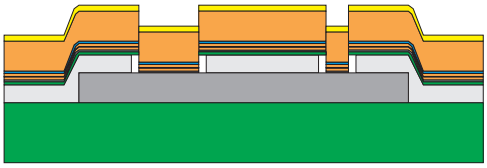

(e) Magnetic layers were deposited.

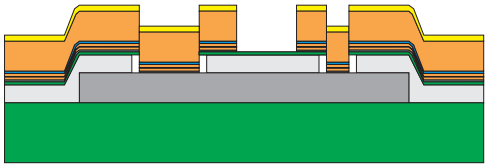

(f) The magnetic layers were etched after optical lithography to form the top contact leads.

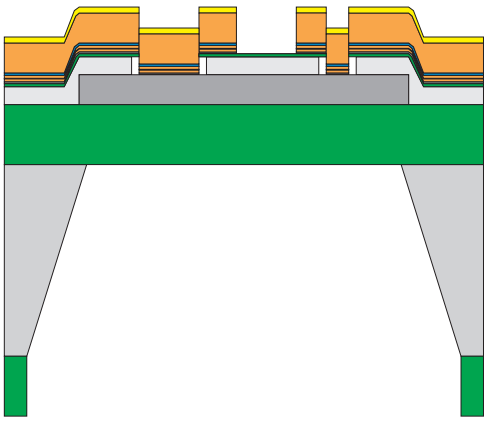

(g) The bottom Si_3N_4 was patterned using optical lithography and the Si wafer was etched in KOH to form a free standing membrane window.

Figure 4.1: Processing steps to make stencil samples.

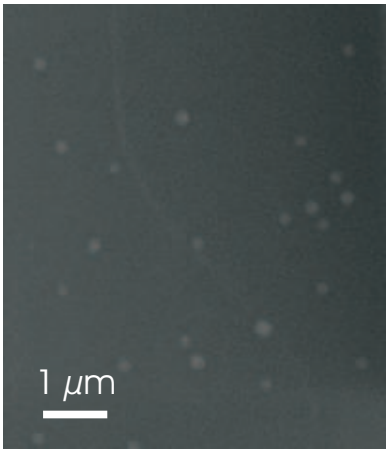

Figure 4.2: Particulate contaminants in the CVD deposited Si_3N_4. They posed little problem due to the low probability that one would occur on the exact site of the pillar.

deposition (CVD) tends to be very smooth and of high quality. However, in some experiments, particulate contaminates in the furnace tube contaminated the nitride as shown in figure 4.2. They were reported by a number of users at SNF and were probably the result of too high a dichlorosilane ($SiCl_2H_2$) flow in the furnace [55]. However, for this project, the contamination was not a problem because only a small area of interest needed to be particulate free.

The backside was then patterned using standard lithographic techniques. After priming the wafer with hexamethyldisilazane (HMDS) in the Yes oven for better adhesion, it was coated with 1.7 μm of Shipley AZ3612, a standard positive photoresist. This is thicker than the resist used later because this layer acted as an etch mask and high resolution was not needed for the backside etch. After exposure and developing, the backside was etched in a plasma etcher to remove the Si_3N_4. This window in the Si_3N_4 would later allow the Si wafer to be etched in potassium hydroxide to form a free standing membrane as shown in figure 4.1g

Next an optical lithography step defined the lower contact of the pillar. After a bilayer resist of LOL2000 and Shipley AZ3612 was spun, the photoresist was exposed and developed. Although AZ3612 is photosensitive, LOL2000 is not. However, it is readily dissolved in developer and formed the cavity in the lower layer of the lift-off

structure. The purpose of this undercut was for efficient lift-off upon metal deposition.

Afterwards, the resist was manually developed in LDD26W developer for 55 s. Although CIS has the capacity to do this automatically on the SVG developer, large areas of the bilayer resist did not clear well when using the automated track. However, for the prior step, where the process was only on a single layer of resist, the SVG developer was completely sufficient.

Next Cr/Pt was deposited to form the bottom contact. The Cr formed a sticking layer and the Pt formed the bulk of the contact. Generally the Cr was about 1.5 nm thick and the Pt was 100 nm thick. Finally, the excess metal was lifted-off in acetone. The sample quality improved greatly with patience during this step. The best results were obtained when the sample sat in acetone for several hours before moving it through a series of methanol, isopropanol, and LDD26W, which was the same developer used previously. However, care must be taken with LDD26W as it readily etches Al, Co, and Cu. While it may also etch other metals, Pt seems to be immune so it could be used in this step. An ultrasonic bath was also occasionally used to remove areas that did not clear well using chemicals alone. However, ultrasonic baths tended to produce small particles of metal that could redeposit onto the sample. Excessive ultrasound also delaminated the Pt contact from the substrate. As such, ultrasound was used with caution on these samples.

Next insulating layers of SiO_2 and Si_3N_4 were deposited over the entire structure using a plasma enhanced CVD process. This was done using a plasma enhanced chemical vapor deposition (PECVD) system at 350 °C. Generally, the SiO_2 was 60 nm thick and the Si_3N_4 was 10 nm thick. Although this is normally considered a low temperature process, the heating was sufficient to cause alloying of some metals. In the first round of fabrication, the lower layer was made of an aluminum/platinum bilayer. The idea was that the Al had good conduction properties while the Pt would protect against oxidation. However, when placed on the 350 °C heating plate in the PECVD system, the two metals alloyed and delaminated from the substrate.

Vias were then patterned using electron beam lithography. 950k molecular weight, 2% polymethyl methacrylate (PMMA) was spun on the sample at 5000 rpm for 40 s. The PMMA was cured for 2 min at 200 °C. Next the PMMA was patterned using

electron beam lithography. After many trials, the best dose was determined to be 0.4 fC for single dots and 0.04 fC for double dots separated by 100 nm. The sample was developed in 1:3 MIBK:IPA (Methyl iso butyl ketone : isopropanol) for 30 s.

Next the sample was exposed to a Si_3N_4 plasma etch in order to transfer the pattern from the PMMA to the underlying Si_3N_4. By isotropically etching the SiO_2 in hydrofluric acid, an undercut was formed below the Si_3N_4. At this point the stencil had been constructed, but the metals for both the pillar and the contacts had not been deposited.

Afterwards another lift-off resist layer was spun on the sample. The process was the same as that used to pattern the lower contact. After the photoresist was patterned, the metals were deposited in the Kobe chamber (see section A.2). The general structure was Cr 1 / Cu 5 / Co 10 / Cu 10 / Co 2 / Cu 10 / Pt 2 (all thicknesses are in nm), but the exact numbers varied depending on the exact sample. These layers filled the pillar and also formed the contacts and waveguides to the pillar. In order to pattern the top magnetic films into the leads, a final optical lithography and ion-milling step was done. Unlike the prior optical steps, this was a single layer, non-lift-off process.

Although the magnetic materials did not contribute as usefully to the lead structure as they would have if they were made of pure Cu, the combination of filling the pillar and creating the leads simplified the processing. However, this also made the electrical analysis more difficult because in-plane GMR obscured the spin injection signal.

The final step was to backside etch the Si wafer so that the pillar structure was sitting on a free-standing membrane. This was necessary the samples were measured in transmission. In order to protect the pillar structures during the wet etching process, Apiezon black wax was used to protect the front side of the samples. It was then removed using acetone.

4.1.2 Forming the Undercut

Pt Mask

The undercut was a crucial step when forming stencil samples. Although it initially appeared to be a simple task, much time was devoted to overcoming difficulties associated with the undercut. The undercut formed a cave where the metals could be deposited without having problems with coverage on the side walls as shown in figure 4.3. Without this undercut, some current would be shunted through the sidewalls and not pass through the sensor layer. Also, this would cause a poorly defined magnetic state at the edges, which could cause the pillar to couple to the magnetic layers outside the pillar region.

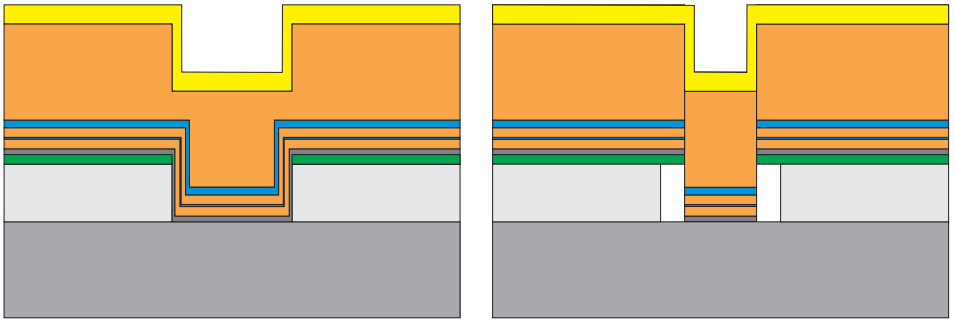

(a) Without an undercut, the layers are continuous and couple to the magnetic regions outside the pillar.

(b) With an undercut, the layers are better defined and all the current must flow from the reference layer through the sensor layer.

Figure 4.3: Comparison of the expected structure with and without an undercut.

The mask layer was initially made of platinum. Pt appeared to have ideal chemical properties: it is robust, mechanically strong, and chemically resistant to hydrofluoric acid, which was used to etch the silicon dioxide. However, one serious problem was overlooked – redeposition on the resist side walls during etching. The etching was done with an argon plasma (MRC etcher, 15 sccm of Ar, 50 W, 5 mT, 6.5 min). As shown schematically in figure 4.4, a spike of Pt, often referred to as a crown, was left around the opening in the masking layer once the PMMA was removed.

Figure 4.5 shows a STXM image of the oxidation of the uppermost copper layer

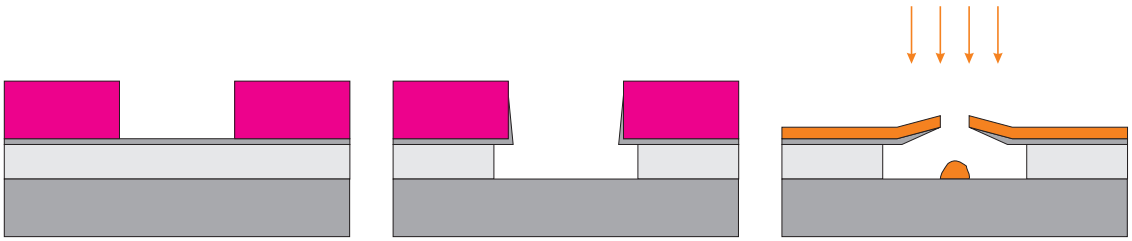

(a) Initially the PMMA is patterned using e-beam lithography

(b) Ar sputtering of the Pt transfers the pattern but also causes redeposition of the Pt on the PMMA resist. However, a hole still exists that allows the HF to etch the underlying SiO_2.

(c) The Pt crown is unstable and sometimes partially obstructs the hole during deposition.

Figure 4.4: Pt proves to be a poor mask for the SiO_2 etch due to redeposition of Pt on the PMMA resist.

around the pillar. Along three edges, the copper appears oxidized. Since the metals were deposited at a 30° angle to normal, one would expect that the Pt crown would preferentially shield one side of the thick Cu from having the proper Pt cap.

Finally, the samples were cross sectioned in the FIB. As can be seen in figure 4.6, the oxide was etched which indicates that a hole was created in the Pt masking layer. However, the metal did not deposit as desired into the hole. In this case almost no metal entered the hole. Nonetheless, based on electrical conductivity measurements, some holes did partially fill. Although not proven beyond all doubt, the Pt likely formed the crown which then collapsed. Depending on exactly how the Pt crown collapsed, a particular sample may or may not be conducting. However, none showed spin injection and likely all had poor depositions that did not adequately form the desired pillar structure.

Si_3N_4 mask

Next the Pt was replaced by 10 nm of silicon nitride. This could then be reactive ion etched in the MRC reactive ion etcher. The advantage of this method was that the reacted product could be extracted through volatile products and be pumped out of the system with ease. This initially worked well and created a suitable hole in the

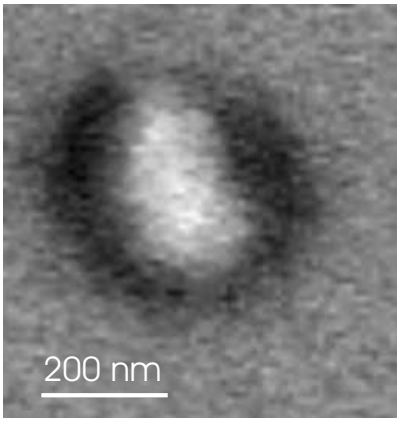

(a) STXM image at the copper oxide edge.

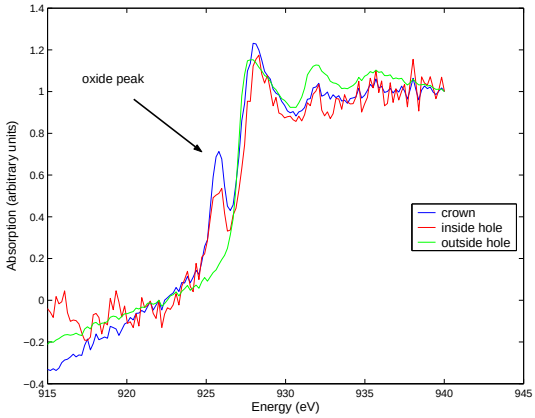

(b) Spectra at the center of the pillar and at the surrounding crown region.

Figure 4.5: Analysis at the STXM shows the pillar and immediately surrounding area are oxidized.

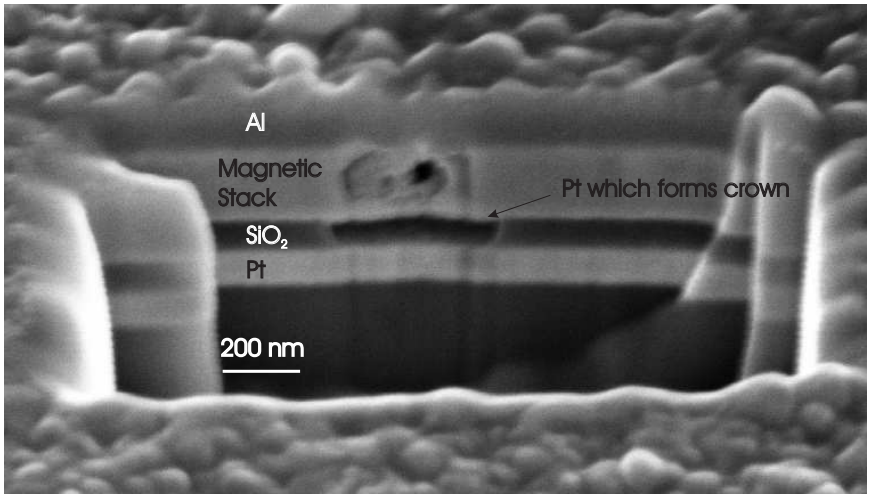

Figure 4.6: FIB cross-section of sample with Pt crown. Although the Pt crown is not clearly visible, its effects are. The hole in SiO_2 was not filled as expected, and the defect in the magnetic layers is most likely caused by the Pt crown as well. The top Al layer was layer deposited to protect the sample during the FIB sectioning.

silicon nitride. However, another unforseen problem soon arose. Although the SiO_2 silicon nitride survived the HF etch and produced an undercut as shown in the SEM image in figure 4.7a, the lift-off and cleaning step produced more problems. Initially, the final contact patterning was to be done using lift-off. These samples were prepared as indicated in appendix B up through and including the etching of the SiO_2 layer with results as shown in figure 4.1d. Next, a bilayer optical photorestist was spun on the wafer. This was then patterned to form a lift-off pattern for the lead structure. The same metals were then to be deposited both in the hole and in the patterned waveguide. However, between the spinning of the photoresist and the deposition, an oxygen plasma was needed to remove photoresist residue in the bottom of the hole that could interfere with good electrical contact between the lower Pt lead and the magnetic materials in the pillar. Thus, an oxygen reactive ion etch was done to clean the hole. However, later analysis showed this partially destroyed the silicon nitride masking layer as shown in figure 4.7b. To further confirm this effect, Al was deposited using the metallica sputter deposition chamber to more easily see if the metal would fill the hole properly. Unfortunately, the Al filled the hole completely as shown in figure 4.7c. Thus, magnetic layers filling the hole in this way would also deposit on the side walls as shown in figure 4.7d and cause a poorly characterized domain state. This could also lead to edges of the two magnetic layers coupling, which would make the samples unusable.

Several attempts were made to overcome this problem. Increasing the thickness of the silicon nitride was considered, but this was abandoned due to the very fast etch rate of PMMA. The 100 nm of PMMA would be etched faster than the silicon nitride and would no longer form a good masking layer. In order to test whether the lithography step or the plasma caused the deterioration of the undercut, a modified process was attempted. The lithography was patterned after the Si_3N_4 etch but prior to the HF etch. For a test, the hole was again filled with Al and cross sectioned as shown in figure 4.8. The resulting structure looked excellent. However, further electrical tests showed shorts within the sample. This was probably caused by pinholes in the Si_3N_4. In the previous samples, the PMMA still remained intact during the HF etch and would protect the oxide below any pinholes. However, in this new process,

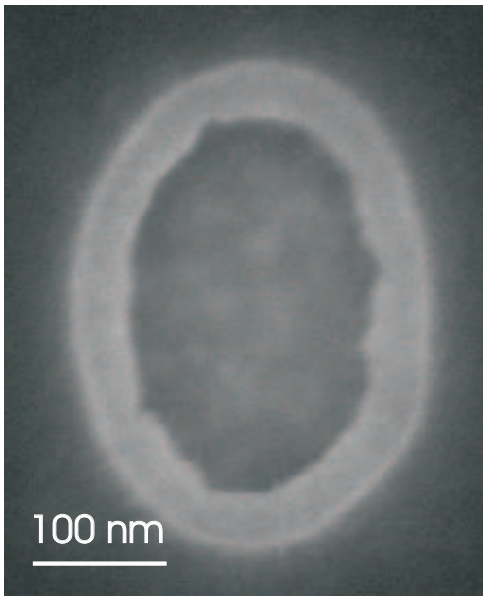

(a) SEM image of the undercut in Si_3N_4 mask over SiO_2 hole prior to cleaning with an oxygen plasma.

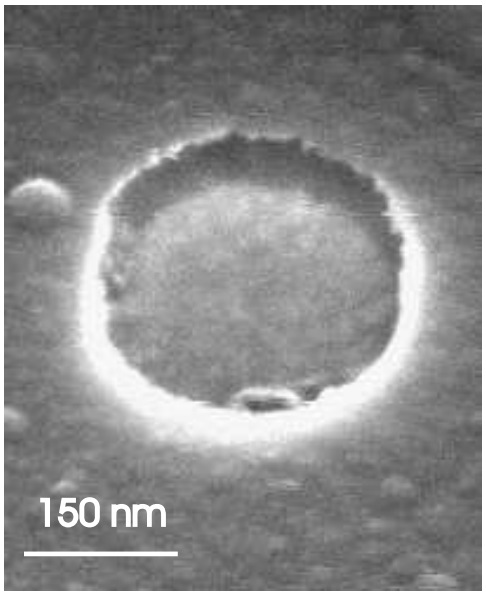

(b) SEM image of the etched hole in SiO_2 after cleaning. The undercut has been destroyed.

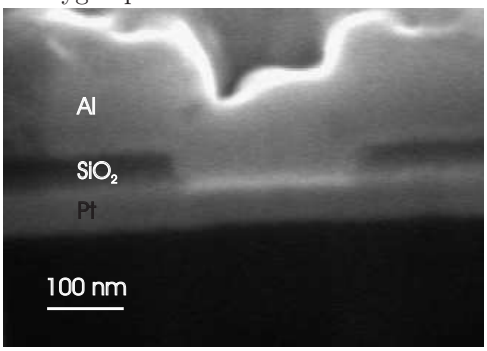

(c) After filling the hole with Al as a test, the sample was cross-sectioned. A pillar was formed, but no undercut is visible.

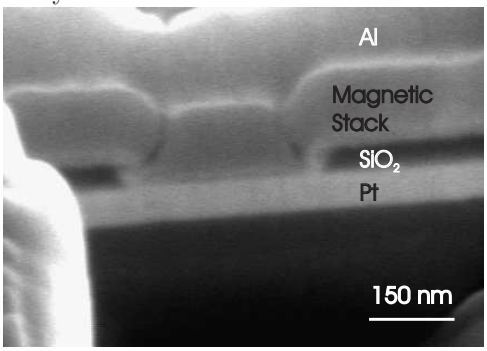

(d) Results when magnetic layers are deposited in the hole after attempting to use bilayer photoresist for patterning the top contacts by lift-off. The hole fills, but without the undercut, the pillar flares near the edge.

Figure 4.7: The Si_3N_4 undercut was destroyed by the oxygen plasma.

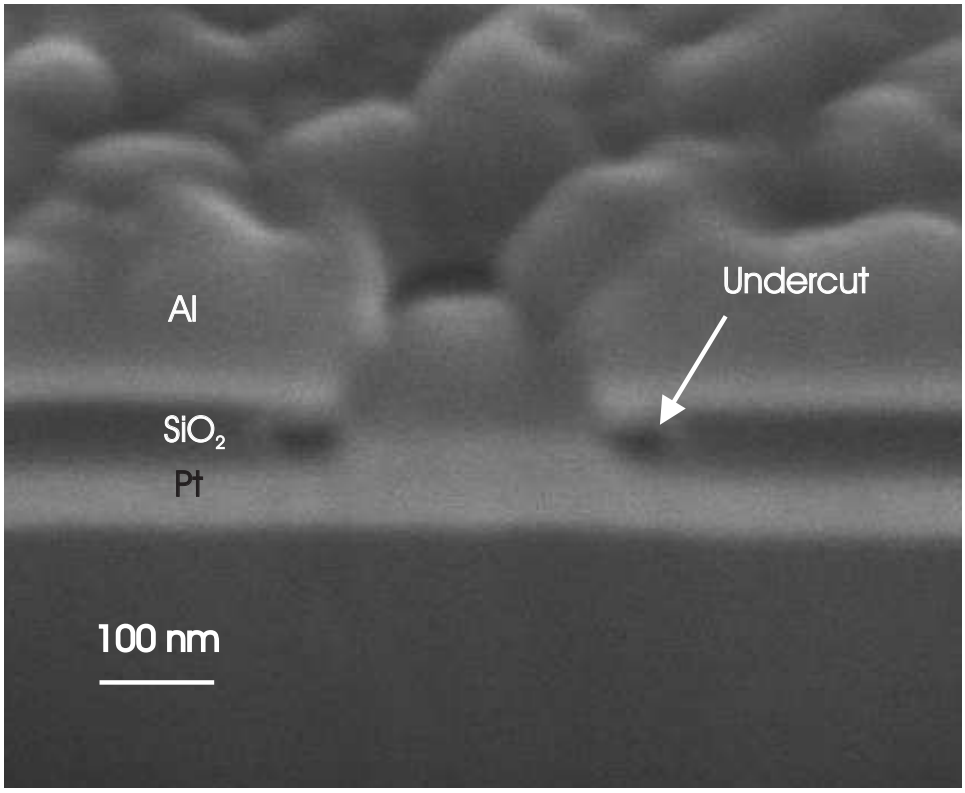

Figure 4.8: Pillar formation when undercut is maintained in reverse lithography process

a larger area around the pillar had to be left uncovered because the lift-off was done by optical lithography which has much poorer resolution than e-beam lithography.

Then the final solution was found: avoid the entire issue. Previously, we had worked to find a way to pattern the metal by lift-off, but it could also be patterned after deposition by Ar sputtering. The silicon nitride and silicon dioxide were etched as before. However, the metal layers were then deposited without ever spinning the photoresist. The pillar was protected with patterned photoresist and the entire wafer was etched in an Ar plasma. Lead lines were then patterned using optical lithography. This added an extra etch and lithography step, but eliminated all the concerns about breaking the undercut before the deposition.

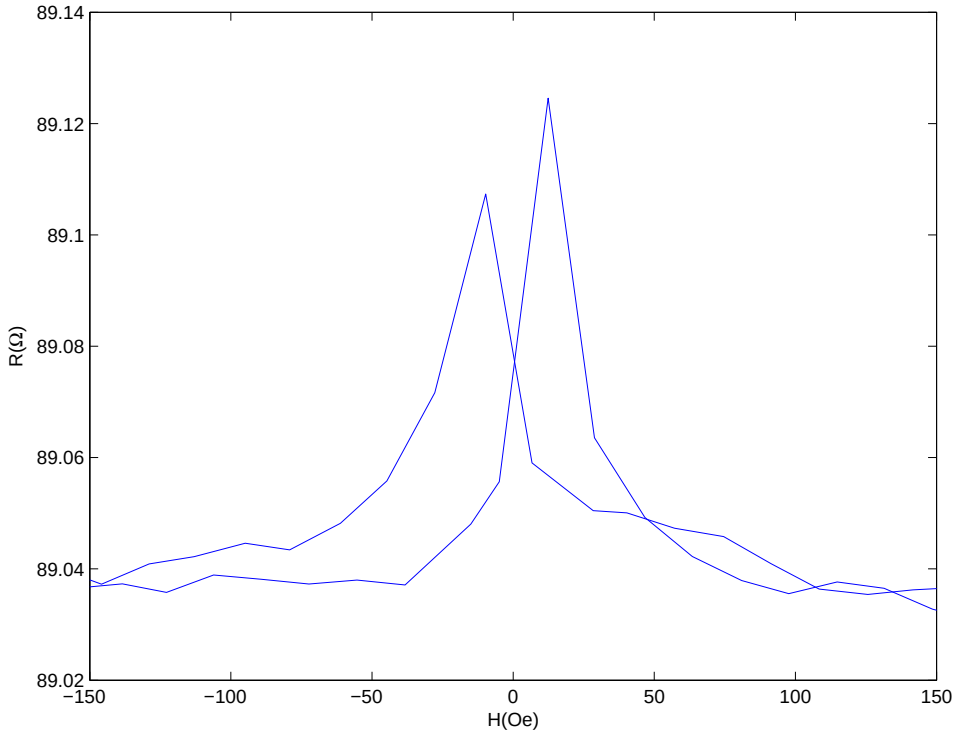

Figure 4.9: GMR measurements of stencil samples. The resistance signal includes switching of the leads and indicates that the sample is properly conductive and the magnetic layers are not coupled.

4.1.3 STXM and Electronic Measurements

In order to further characterize the samples, several electrical tests and STXM measurements were made. The most obvious idea was to conduct GMR and differential resistance verses applied current. Typical GMR measurements are shown in figure 4.9. Electrical spin injection measurements, dV/dI vs. applied current, showed no signal. However, this is not surprising. The GMR signal shown includes a large component from the switching in the lead. In order to simplify the processing, the top leads were made of the same magnetic material as the pillar as shown in figure 4.1g. However, the magnetic layers contained in the leads would still switch in a magnetic field and would not switch through spin-torque transfer. The small CPP-GMR signal of the pillar would be too small compared to the CIP-GMR signal.

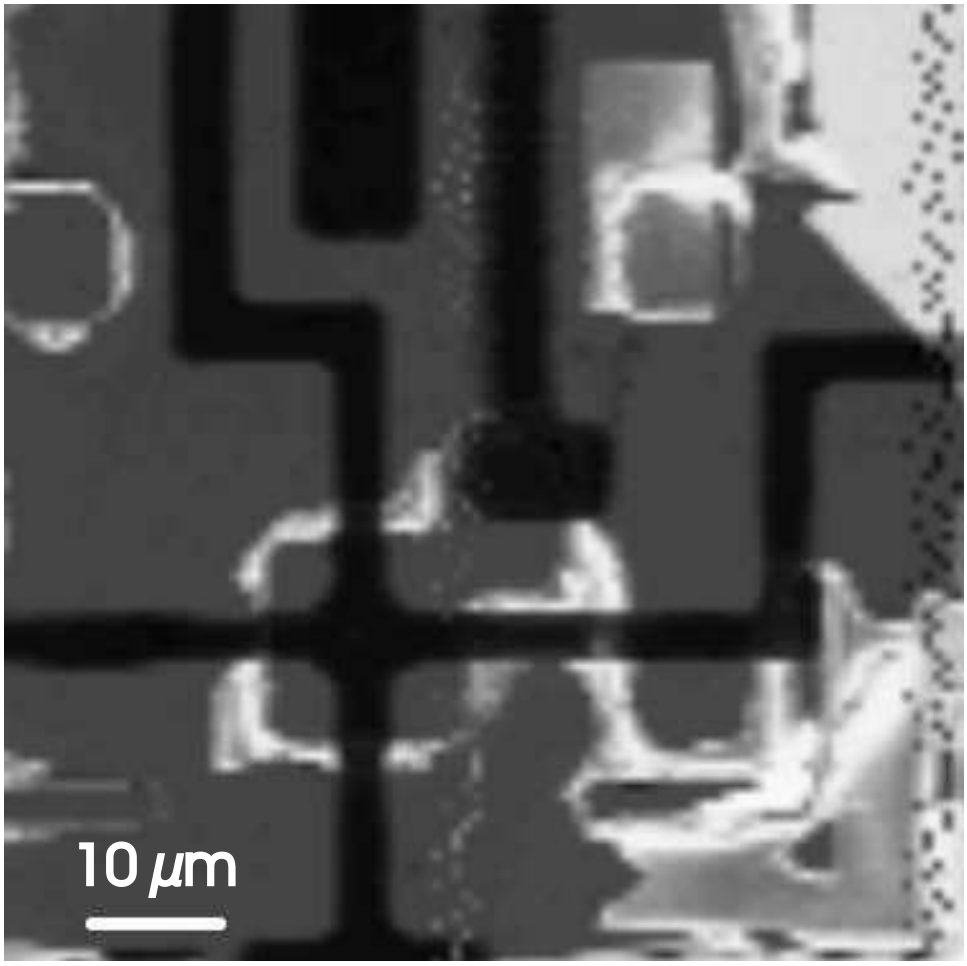

Figure 4.10: Due to failure of the Apiezon wax used to protect the wafer during the last KOH etching step, many samples were completely destroyed.

STXM measurements on the stencil samples lead to several important improvements, but the present results are still inconclusive. After solving the crown problem, the samples appeared viable and in good condition. Unfortunately, due to problems with the black wax used during the final processing step, almost all of the samples were destroyed. The wax flowed at a much lower temperature than observed previously and in other batches of wax tested subsequently. Thus, it was concluded that the wax was probably mislabeled when it was purchased. As such, only a few non-ideal samples survived. Many were destroyed by the KOH and produced structures such as those shown in figure 4.10.

A full characterization of this set of samples was not possible during the limited time available at the STXM. Because the subtractive samples discussed in the next chapter more quickly yielded good results, most of the available beam time was used on these samples. More beam time will be needed for a full characterization. However, some useful results were obtained during the last experiment. Figure 4.11 shows an overview image on the Co edge.

Also, the Co within the hole was estimated to be at least 90% of that outside the pillar. Current was also shown to pass through the pillar. Figure 4.12 shows the switching when the sample was pulsed. Unfortunately, spin injection was not clearly visible. However, no sample could be tested in great detail due to time constraints and the low yield caused by the failure of the Apiezon wax. Further testing is necessary to confirm the integrity of these samples and to conclusively show spin injection.

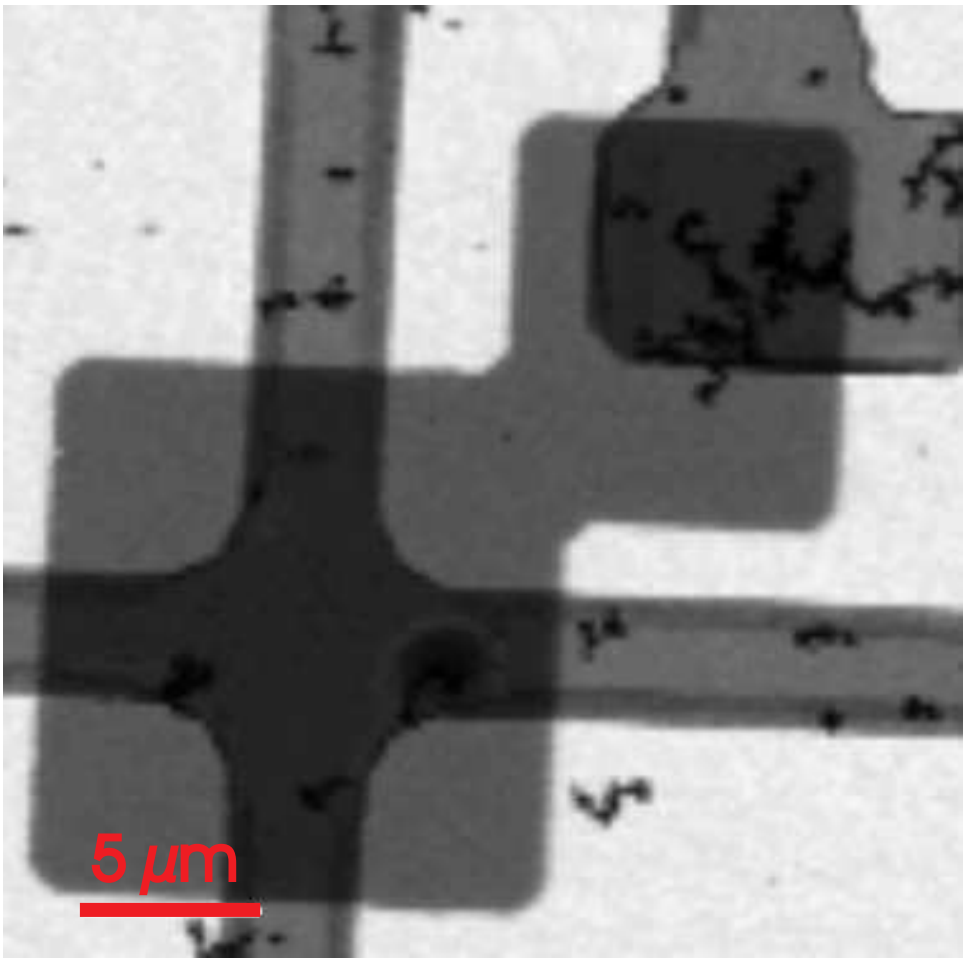

Figure 4.11: An overview of a stencil sample. The cross is the top contact while the two connected rectangles are the lower Pt layer. The black beads are contamination from incomplete removal of the black wax. They have no effect on the electrical or magnetic properties of the sample. The pillar is located at the center of the cross.

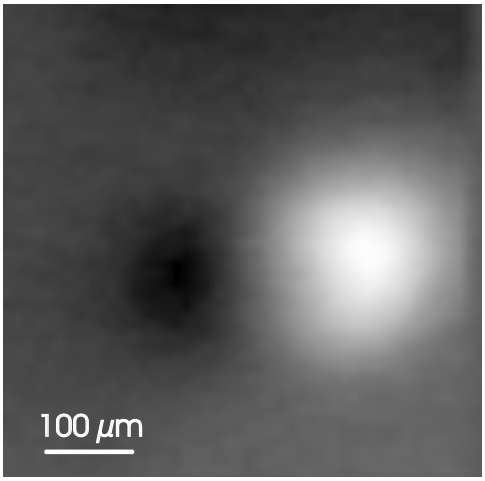

(a) STXM image of hole while current is pulsed through the sample. Most of the contrast is due to thickness differences. The center of the pillar is offset between the black and white areas caused by the undercut and pillar being imaged at a tilt.

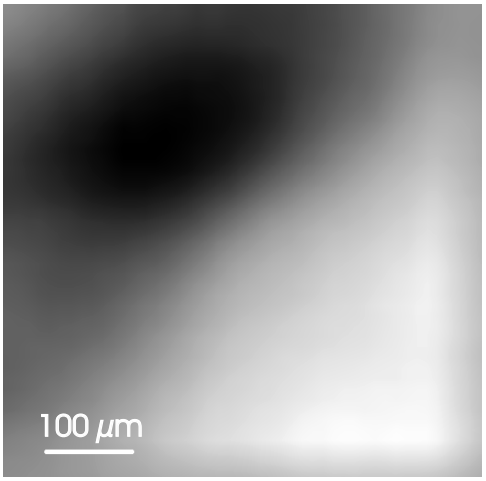

(b) Ratio of the hot/cold pulse images. Black and white areas represent areas that showed magnetic excitations caused by the current pulse. Based on the asymmetry of the regions and the fact that they primarily lie outside the pillar, this is most likely caused by Oersted fields.

Figure 4.12: STXM images of a stencil sample (Ti 5 nm / Cu 10 nm / Co 2.5 nm / Cu 10 nm / Co 8 nm / Cu 100 nm / Au 20 nm) at the Co L_3 edge. The sample was mounted at 30° and circularly polarized x-rays were used. The pulse was a 500 mV excitation pulse (hot pulse) followed by a -500 mV reset pulse (cold pulse). This corresponded to approximately 2.7×10^7 A/cm^2. Prior to pulsing the sample, the sample was set in a parallel configuration state. The applied current was directed such that electrons passed from the thin layer to the thick layer.

4.2 Subtractive Samples

4.2.1 Processing

The subtractive processing method was more reliable but less flexible than the stencil method of preparing samples. All samples of this type were generously prepared by Jordan Katine at Hitachi Global Storage Technologies. Further details can be found in [56, 33, 2]. The description below and figure 4.13 show the main steps and provide the proper end result. However, several proprietary steps have been withheld.

First, the magnetic multilayers were deposited and capped with tantalum and ruthenium. In all experiments done to this point, the stack sequence was Ta 50 / Cu 500 / Ta 50 / PtMn 200 / $Co_{.86}Fe_{.14}$ 20 / Ru 8 / $Co_{.86}Fe_{.14}$ 20 / Cu 35 / $Co_{.86}Fe_{.14}$ 10 / NiFe 35 / Cu 200 / Ru 20 / Cr 50 / Cu 1400 / Au 100, where all thickness are measured in Å. The lowest three layers formed the bottom contact. PtMn is a antiferromagnet used to exchange bias the $Co_{.86}Fe_{.14}$. The $Co_{.86}Fe_{.14}$ / Ru / $Co_{.86}Fe_{.14}$ trilayer formed the reference layer that polarized the electrons and did not switch. These three layers together formed a synthetic antiferromagnet which has almost no stray field that could bias the sensor layer. The 35 Å of Cu acted as the spacer layer that kept the reference and sensor layers from exchange coupling together. The $Co_{.86}Fe_{.14}$ / NiFe bilayer formed the sensor layer that switches during these experiments. Finally, the Cu / Ru / Cr / Cu / Au structure formed the top contact and cap. After depositing the entire stack of metals, the samples were annealed at 250 °C in a 13 kOe field for 5 hours in order to set the PtMn and $Co_{.86}Fe_{.14}$ layers.

Next two lithography steps were done. The first was a lift-off of Ta 100 Å / Au 1000 Å to form alignment marks on the wafer. The second lithography step was used to protect the bottom lead from the subsequent ion mill which removes part of the the bottom lead material. This minimized the capacitance between the bottom and top leads. The milled areas were then refilled with 1100 Å of aluminum oxide using ion-beam deposition. Lift-off then removed the excess aluminum oxide.

The pillar was defined using e-beam lithography. A negative resist (Hydrogen SilsesQuioxane: HSQ) was used to create the desired pattern structure. The HSQ was sufficiently hard to survive ion milling of the magnetic devices. In order to verify

the progress of the mill, secondary ion mass spectroscopy (SIMS) was used to monitor the milled species. After ion milling, more aluminum oxide, usually about 1000 Å, was deposited via ion-beam deposition.

In order to remove the resist and create a self-aligned via to the pillar, chemical mechanical polishing was used. Next photolithography was used to pattern a 2 μm area on top of the pillar, followed by 1000 Å of alumna that was deposited and lifted-off. This layer minimized the potential for shorts between the bottom and top leads.

In order to contact the bottom lead, photolithography was used to pattern vias in the alumina followed by etching in Ethylenediaminetetra acetic acid (EDTA). After stripping the resist, a brief oxygen reactive ion etch cleaned any organics from the surface of the wafer.

Finally, the top lead was deposited. After ion milling through the Ta/Ru cap and into the Cu above the free layer, Cr 50 Å / Cu 50 Å / Au 50 Å / was ion beam deposited. In order to pattern the top lead, photoresist was spun and patterned, and the excess material was removed by ion milling.

4.2.2 STXM and Electronic Measurements

The subtractive samples were characterized in a similar manner to the stencil samples. Due to time constraints of available beam time and a processing problem at Hitachi, only 400 nm × 400 nm samples were available at the time of these measurements. Typical GMR measurements are shown in figure 4.14. Unlike the stencil samples, the only GMR signal was from the pillar itself. Also, the reference layer was exchange biased by the underlying antiferromagnet. Thus, only one transition is visible.

Besides GMR measurements which show that the sensor layer is switchable, a pump-probe experiment was performed as previously described in section 2.2.2. For all the measurements shown below, the current passed through the sample was 40 mA, which roughly corresponds to a current density of $1.5 \times 10^7 \mathrm{A/cm^2}$. The current direction was such that electrons passed from the bottom of the pillar to the top. This corresponds to electrons passing from the reference layer to the sensor layer.

When considering the effects of the pulsing sequence, there are four main stages

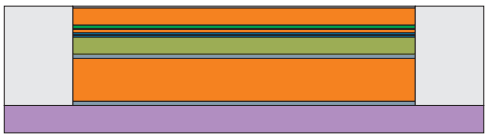

(a) Magnetic layers are deposited, annealed, and patterned using photolithography and ion milling

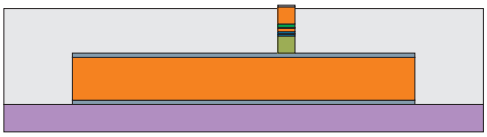

(b) E-beam lithography and ion milling are used to pattern the magnetic pillar. Alumina is deposited by ion-beam deposition, which is then planarized by chemical mechanical polishing (CMP).

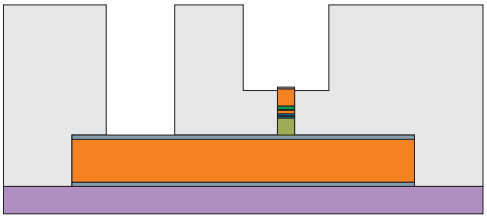

(c) Photolithography is used to protect a region near the pillar. After more alumina is deposited, vias are etched to contact the lower lead.

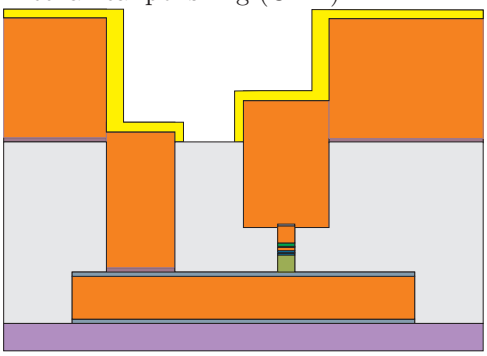

(d) Finally, the top contact is deposited and patterned using more ion milling.

Figure 4.13: Processing steps to manufacture subtractive samples.

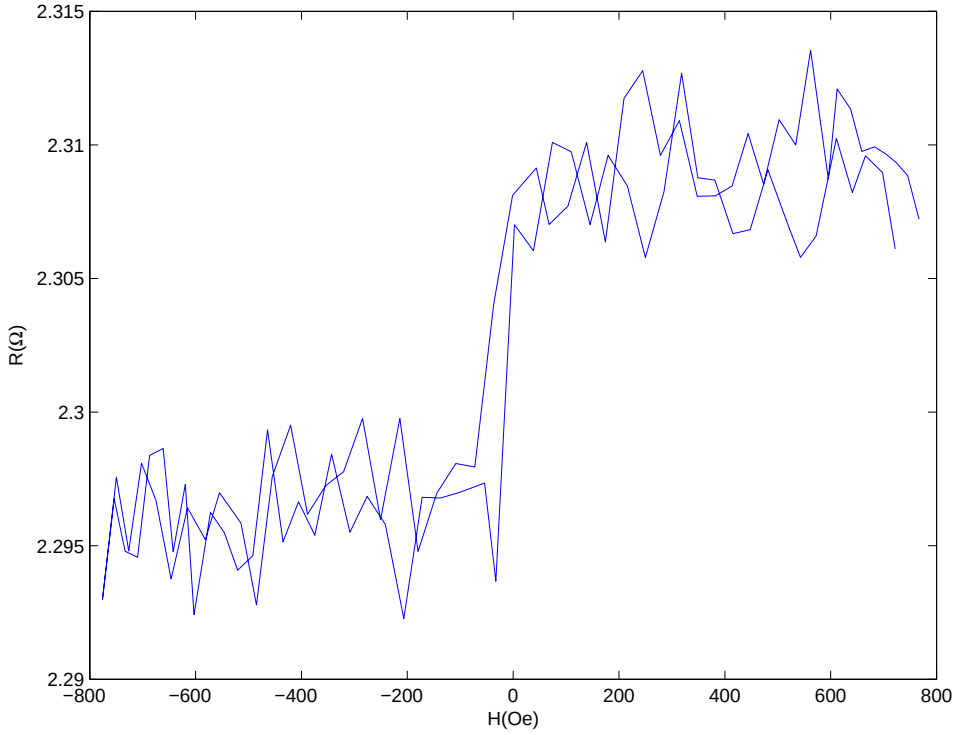

Figure 4.14: GMR measurements of subtractive samples. The reference layer is pinned via exchange biasing to an underlying antiferromagnet. Thus, only one switching event is visible.

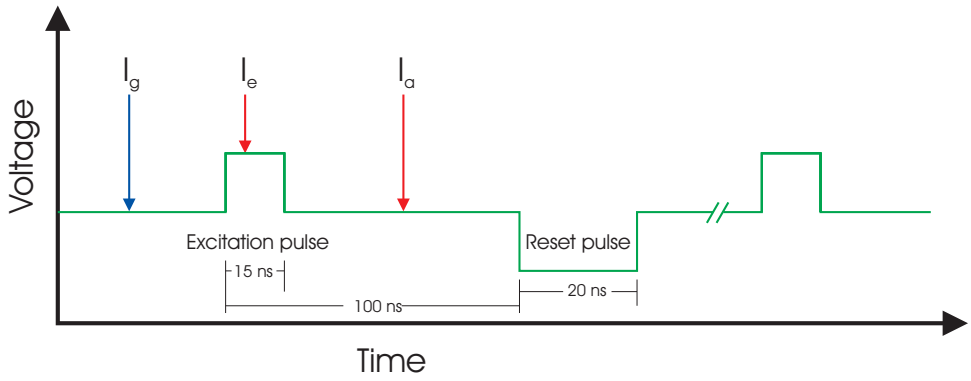

Figure 4.15: The transmitted x-ray intensity, which can later be used to find the magnetic state of the system, was measured in three regions of the pulsing sequence: in the ground state (I_g), during the excitation pulse (I_e), and after the excitation pulses (I_a).

as shown in figure 4.15. The initial state is the ground state. Next the excitation current pulse passes through the sample, and the magnetic state is altered to a non-equilibrium state. A few nanoseconds after the pulse passes, the system will relax. It may or may not return to the initial ground state. Finally, the reset pulse arrives, and the system is again excited. However, due to the opposite polarity of the current, the state is unlikely to be the same as the state during the initial excitation pulse. After the reset pulse passes, the system should then return to another equilibrium state. As this experiment was designed, the last state of the sequence was intended to be the same as the initial ground state. This intent follows from the assumption that the switching behavior was reversible and the current was strong enough to overcome any asymmetry in the critical switching current from spin injection. As will be shown shortly, this assumption appears to have been valid.

Some thought must be invested to determine how to best extract the proper magnetization contrast from each image. First, some information must be known about the ground state. Attempts were made to measure the ground state by reversing the x-ray polarization and measuring only at I_g. However, this did not work well due to sample drift between the two measurements. Thus, a pulsed experiment was necessary. The leftmost image in figure 4.16 shows the magnetization image of I_a/I_g. This image contains a mixed signal of the magnetic information of the system after

the excitation pulse and after the reset pulse.

In order to better understand these results, some idealized states were simulated as shown in figure 4.17. Finite resolution of the STXM and the fact that all images shown were filtered using a Lee filter [57] to remove noise, caused the actual data to be less sharp than the idealized images. As such, the idealized images were also blurred using a Gaussian filter to better understand how the real images may appear.

If the system was in the same state before and after the excitation pulse, then figure 4.16 would show no contrast for the ground state image. Since this was not the case, the pulses produced a reproducible change. However, determining the exact nature of the change was not trivial. From the simulations shown in figure 4.17, it was unlikely that in practice any of the flux closure states could be distinguished from one another. Thus, no definitive conclusion could be drawn as to exactly which flux closure state is present in these samples. Further discussion will focus on distinguishing a flux closure state, which is favored by Oersted fields, from a uniform magnetization state, which is favored by spin injection.

The cylindrical symmetry of the pillar combined with the uniaxial anisotropy preserves a diad axis or a diad with inversion perpendicular to the surface. Thus, flux closure states with centers not coincident with the center of the pillar are unlikely for the relaxed state. Consequently, states c and e in figure 4.17 are unlikely ground states.

The question now remains as to whether the ground state is a uniform state or a flux closure state. If both were single domain states, then only two regions would exist. The pillar would be either white or black, and the surrounding area would be gray. If one state was a flux closure state while the other was a single domain state, the result in the divided image would show no change in half of the pillar while the other half would switch direction and thus be either black or white. Since two colors are distinctly visible, the two states are most likely flux closure states.

Now that the ground state can be found, we can continue toward the main goal of producing an image of the magnetization state when the pulse was applied. The initial data included topographical signals as well as the magnetic signal. As mentioned previously, this could be eliminated by dividing two images, which yielded the

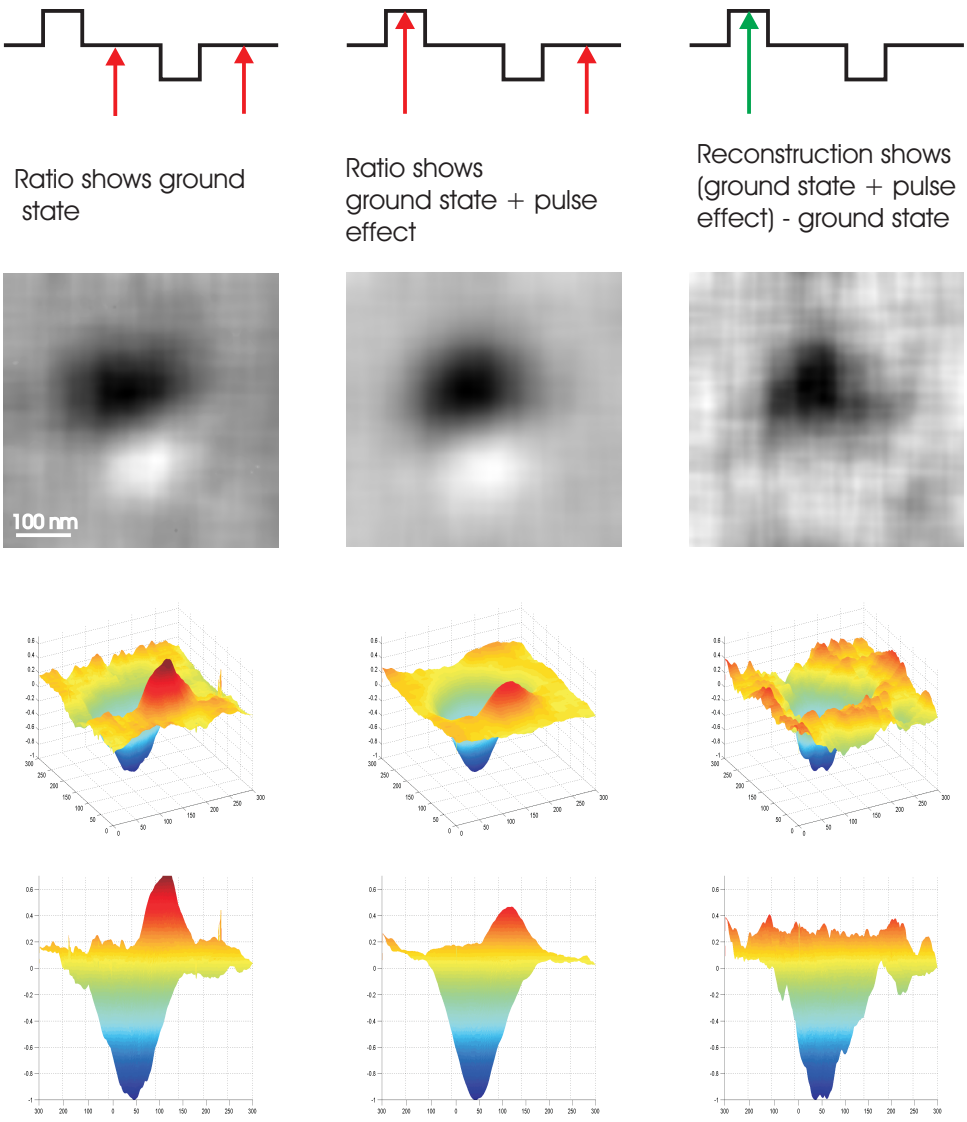

Figure 4.16: Intensity and surface plots of STXM data taken at various times during the pulsing sequence. White and black regions of the intensity plots correspond to red and blue regions in the surface plots, respectively. The first two columns show the ratios at the points in the pulsing sequence designated by the arrows in the top row. For the leftmost column, the two divided states are assumed to be two flux closure states with opposite directions. Thus, this represents twice the real contrast shown in the ground state. The middle image is a mixed signal of the magnetic state during the pulse and in the ground state. By combining these images using equation 4.2, the magnetic state at the pulse can be reconstructed. During the pulse, the white/red region disappears and the black/blue area grows significantly. This is indicative of a spin injection since the pillar is becoming more uniform. However, the fact that the entire pillar does not become black/blue indicates that the Oersted and spin injection effects in this region are nearly compensating each other.

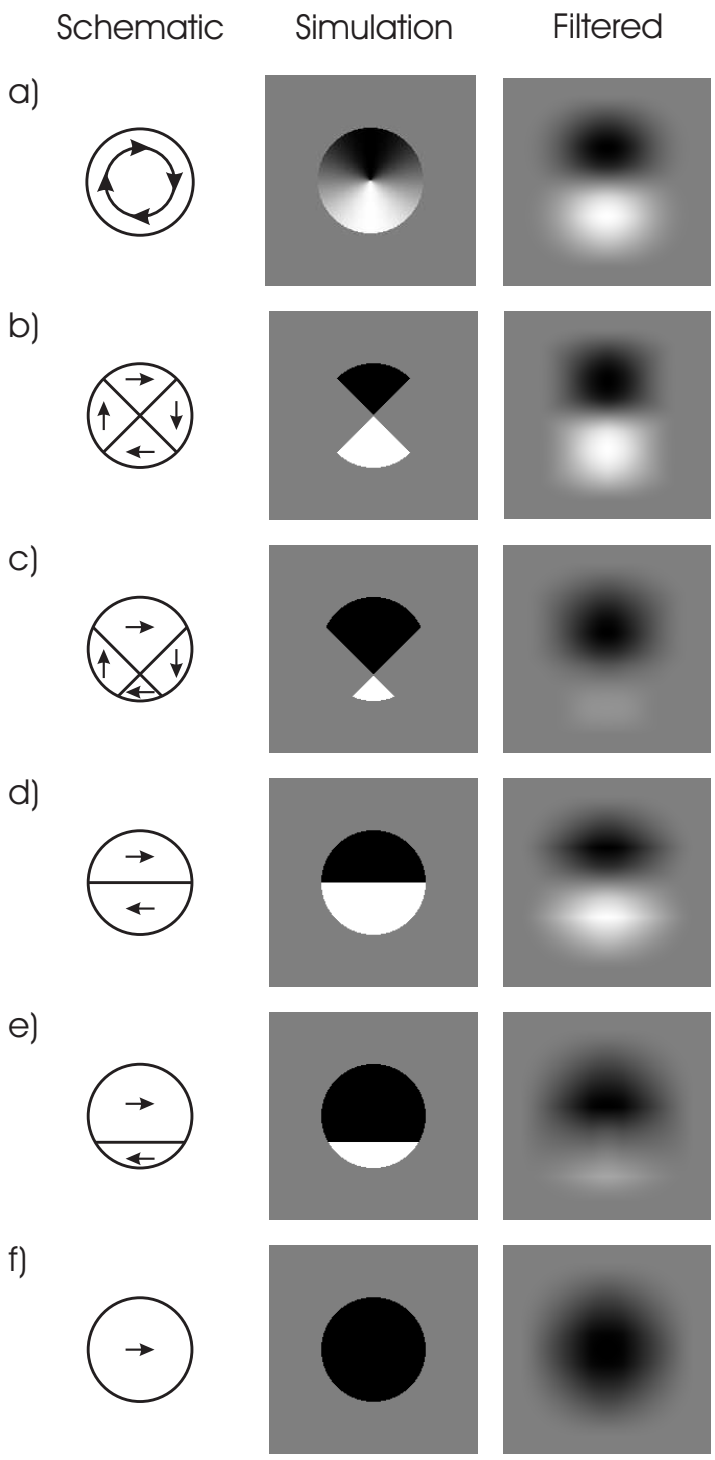

Figure 4.17: Idealized STXM images for various possible states of a magnetic pillar and the effects of finite spatial resolution (simulated using a Gaussian filter). Note that for cases *d*) and *e*) the perpendicular regions of the flux closure state should be relatively small and were neglected in the simulation.

magnetization difference between the states. After this preliminary processing, two sets of data were available.

$$\begin{aligned} M_e - M_g &\propto \tfrac{I_e - I_g}{I_e - I_g} \approx \tfrac{I_e}{I_g} - 1 \\ M_a - M_g &\propto \tfrac{I_a - I_g}{I_a - I_g} \approx \tfrac{I_a}{I_g} - 1 \end{aligned} \tag{4.1}$$

Where M_i is the magnetization signal for state i of figure 4.15, and I_i is the measured intensity of an image taken at time i. Since the magnetization signal after the excitation pulse and in the ground state should be equal and opposite, $M_a = -M_g$. Combining this with the above equation yields

$$M_a \propto \left[\left(\frac{I_e}{I_g} - 1 \right) - \frac{1}{2} \left(\frac{I_a}{I_g} - 1 \right) \right] \tag{4.2}$$

Many images were taken on the pulse, but with slightly different delays. These will be discussed in more detail shortly. However, in order to increase the signal-to-noise ratio, these magnetic contrast images were aligned and summed under the assumption that on average, the magnetic system switched to a new, nonequilibrium state at the beginning of the pulse and did not continue to change drastically during the pulse. Equation 4.2 was then applied to remove the mixed signal from the ground state. The results of this subtraction reconstruction along with some possible idealized states are shown in figure 4.18.

From the constructed image, it appears that the system is subject to spin injection. In the reconstructed image, the light area is no longer visible and the dark area has grown. The growth indicates that in the top part of the picture the spin injection and Oersted fields favor the same magnetization direction, while in the lower region the two effects tend to cancel each other. This is supported by simulations of the expected image if the domain wall separating the two regions moves away from the center of the pillar. Figure 4.19 shows a schematic of the forces on the sample at each point of the pulse sequence.

The final piece of data that can be extracted is some information about the time needed for the system to be excited from the ground state. Figure 4.20 shows the time sequence data in more detail.

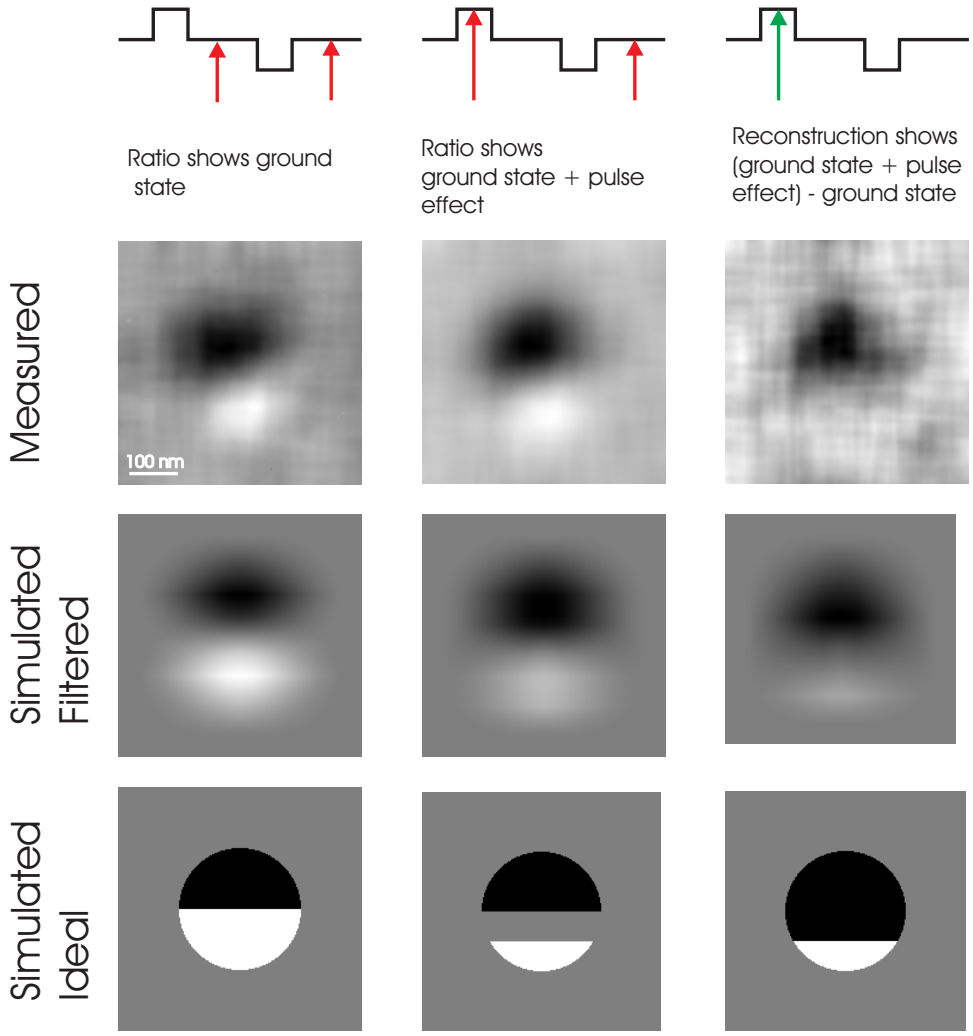

Figure 4.18: The measured data for various time pulses along with simulated data that was then filtered for comparison to the measured data. The pulsed state appears to be a flux closure state with an offset center due to the influence of spin injection which favors a uniform magnetization.

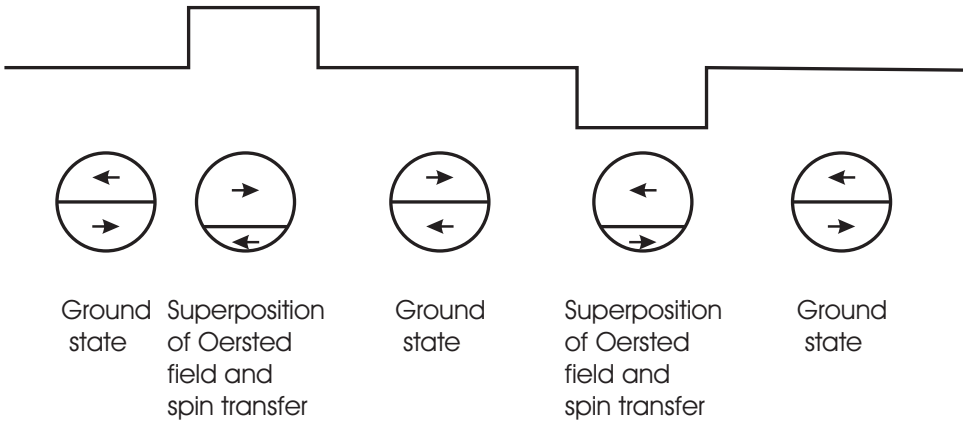

Figure 4.19: The system begins in a flux closure ground state. As the current passes through the sample, there is a superposition of an Oersted field that favors a flux closure state of the opposite direction while spin injection favors a uniform state. The two forces add together to switch the flux closure state while also moving the domain wall to form a more uniform state. The system then relaxes once the current pulse has passed. When the reset pulse arrives at the sample, all effects are reversed and the original ground state returns once the reset pulse has passed.

Prior to the pulse, the pillar appears to be in a flux closure state. After approximately 400 ps the flux closure state switches direction due to the Oersted fields. After 2.71 ns the effect of the pulse appears to have been maximized and the spin injection has caused the domain wall to move away from the center of the pillar. Long after the excitation pulse, the pillar relaxes back into an equilibrium flux closure state. In order to see these effects more clearly, images from each region were averaged and compared to simulated data in figure 4.17 as shown in figure 4.21

Overall, spin injection was imaged for the first time. All other researchers have only been able to perform electrical measurements and have limited data on the time-resolved progression of the magnetization under spin injection effects. However, due to the complex overlay of Oersted and spin injection effects, quantitative measurements have proven difficult. Future experiments are planned on smaller samples of this type that should help reduce the Oersted interaction. As such, a more quantitative understanding should be possible with the continuation of this work.

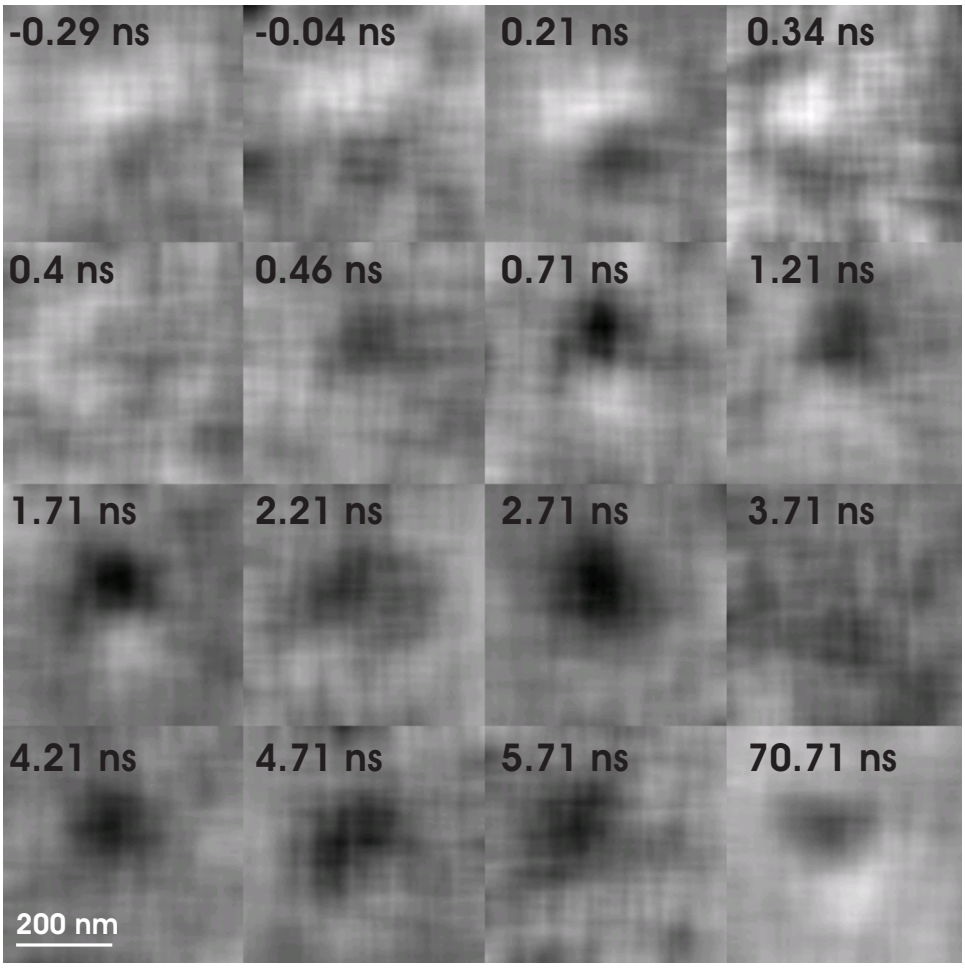

Figure 4.20: The magnetic state before, during, and after the excitation pulse. All images have been enhanced with ground state subtraction. Prior to the pulse, the pillar shows a flux closure state of opposite direction to that in the last image which occurs long after the excitation pulse has passed. During the transition, spin injection helps Oersted switching in the top regions, but cancels its effects in the lower regions of the pillar. The pillar then relaxes back into a flux closure state of the opposite direction relative to its initial state.

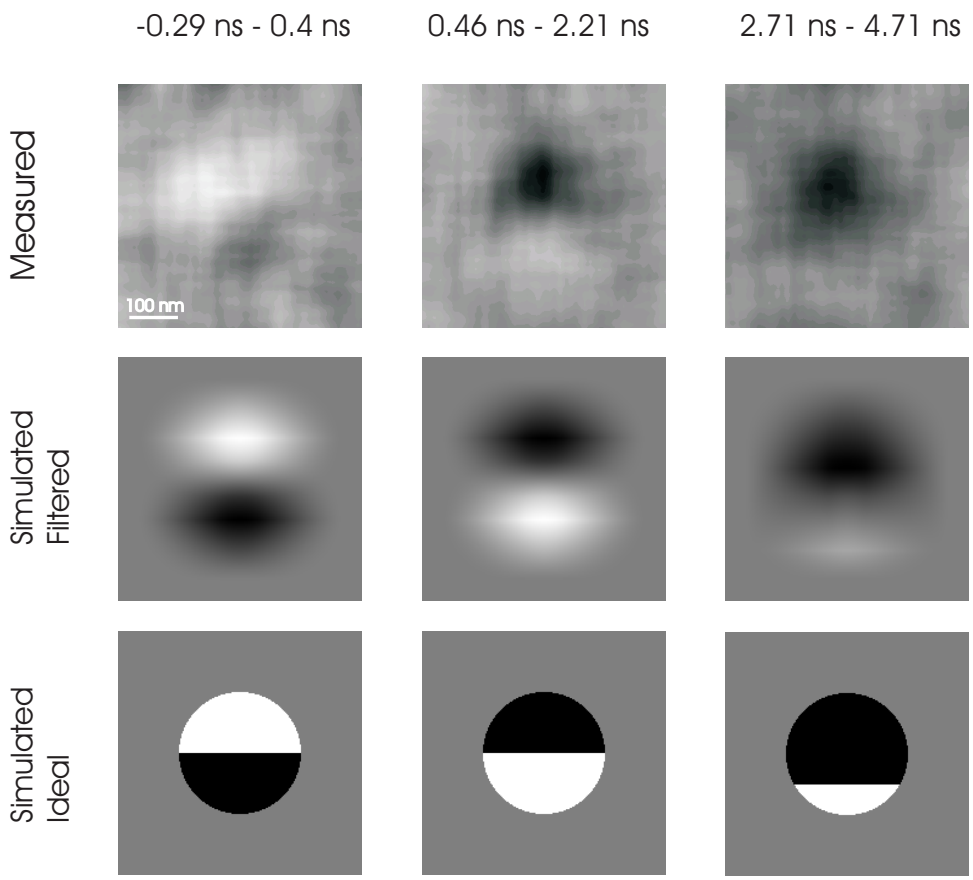

Figure 4.21: Three regions of the magnetic states shown in figure 4.20 were averaged and compared to simulated data. Before the pulse, the pillar was in an equilibrium flux closure state. Initially during the pulse, the Oersted fields switch the direction of the flux closure state. After the main switching event, spin injection moves the domain wall away from the center of the pillar.

Chapter 5

Conclusions

Spin injection has great potential for future technological innovations. Unlike most conventional technology that uses only the electric charge of electrons to process information, a whole new method for storing information can be realized through the understanding of the interaction of spin polarized currents with ferromagnetic materials.

This work concentrated on fabrication issues of creating samples suitable for spin-transfer torque experiments. Initially, samples were fabricated by taking silicon nitride membranes and using a focused ion beam to drill small holes in the nitride. Ferromagnetic and paramagnetic layers were then deposited from both sides. These samples had the advantage of being relatively easy to fabricate, but lacked some of the robustness of lithographically fabricated specimens. Initially, the ferromagnetic reference layer was deposited on the backside of the sample, but stray fields from deposition on the side-wall of the silicon window made this configuration unusable. To correct this deficit, an all-front-side configuration was used. In these samples the current was concentrated in Cu pillars that had been created by depositing paramagnetic material in the silicon nitride holes. This configuration required that the spin polarized current diffuse through the reference and sensor layers. Due to magnetic uniformity issues, spin injection could not be clearly resolved in these samples. However, Oersted fields were clearly visible.

Next, two new types of samples were created. In the first sample type, a stencil

process was used. These samples relied on a multistep process whereby an undercut was made in a silicon nitride masking layer located on top of silicon dioxide. These samples had the advantage that once a large number of stencils were created, many different layers could be tested to find the most ideal configuration. Many problems needed to be solved in order to manufacture these samples. All known issues have been solved, and the samples have been preliminarily tested. However, because magnetic materials were used in the leads, electrical measurements cannot accurately measure spin injection effects. Limited STXM time and the high loss of samples due to failure of Apiezon black wax in the last batch has limited the characterization of these samples to date. At this time, they look feasible, but no spin injection has been clearly observed in them.

The final samples were created using a subtractive method. All the layers were deposited initially, and then a series of lithographic and etch steps removed the excess material. Limited STXM time again restricted the complete characterization of these samples. Nonetheless, spin injection has been clearly observed in these samples. This is the first time anyone has directly imaged spin-transfer torque. However, quantitative measurements of this phenomenon are still quite limited due to the fact that the spin injection signal is combined with Oersted switching. Further experiments are planned on smaller samples that should allow a clearer observation of the spin injection signal using the same methods.

The goal of this project was to fabricate and image devices that demonstrate spin-transfer torque. Although this goal has been achieved, much work remains before the time dependence of the interaction is fully understood. As the underlying physics of the interaction of spin polarized currents with ferromagnetic materials is more fully explored, it hopefully can be harnessed for technologically important commercial devices.

Appendix A

Equipment

A.1 CIS equipment

- Diffusion wet bench (wbdiff): Wet bench used for cleaning wafers before low-pressure chemical vapor deposition (LPCVD) of Si_3N_4. Standard clean process: 10 minutes in H_2SO_4:H_2O_2 (4:1) @ 90°C. Rinse. 10 minutes in H_2O:HCl:H_2O_2 (5:1:1) @ 70°C. Rinse. 15 seconds in 2% HF @ room temperature. Rinse. Spin dry and test the resistivity of the rinse water $>$ 16 MΩ cm.

- Yes oven: Yes LP-111 oven. Deposits a thin layer (few angstroms) of hexamethyldisilazane (HMDS) as a sticking layer under resist. The deposition is under low vacuum (about 1 torr) at 150°C.

- Tylan nitride: Low-pressure chemical vapor deposition (LPCVD) furnace used to deposit low stress Si_3N_4. In this work, recipe LONH378 was used, which grows the nitride at 800 °C in 250 mTorr of dichlorosilane ($SiCl_2H_2$) and ammonia (NH_3).

- Karl suss: Karl Suss MA-6 Contact Aligner. 1:1 magnification. Capable of front and back side alignment. Hard contact, soft contact, high vacuum, low vacuum and proximity contact are all possible. In this work, hard vacuum contact is always used except for backside alignment, where the vacuum contact mode is

not important due to the large features not requiring it. The Karl Suss aligner can take pieces or wafers up to 4". The masks are 5" and are usually made in house. The resolution is approximately 0.75 μm in the vacuum contact mode.

- Metallica: a DC magnetron sputtering system. Base pressure: 10^{-7} Torr. Roughing pump: Edwards E2M80. High-vacuum pump: Airco Cryogenic pump. Process gas flow: 30 sccm of Ar. Sputter sources: two "US GUN" magnetron S-Gun sputtering sources, each of which uses 1" x 1/8" targets. Water cooling is in direct contact with the gun magnets. Most conducting, non-magnetic metals can be readily sputtered with this system. The system can hold four 4" wafers. However, one wafer position is typically reserved for a dummy wafer. Each wafer and each material on each wafer is individually deposited. Thus, co-deposition is not possible. The deposition is in normal incidence with the sputter guns located directly below the wafer.

- MRC etcher: MRC Model 55 RIE Etcher. Diffusion pumped, plasma reactive ion etching system for pieces and wafers up to 6". Gases available: O_2, CF_4 (Freon 14), Ar, SF_6, or CHF_3 (Freon 23).

- drytek1: Drytek 100 plasma etcher. Used for etching nitride, poly, Ti, Si and resist. Contains one etch electrode and uses SF_6, $CHClF_2$, CF_3Br, CF_4 and Oxygen.

- SVG coater and developer: Automatic photoresist and and developing tool manufactured by Silicon Valley Group, Inc. Capable of spinning 25, 4" Si, glass, or quartz wafers in a batch. Fitted with a prime oven, which dispenses HMDS, and a pre-bake oven. Uniformity of spun photoresists are ±100 Å. Developer tool has spin station for cleaning wafers and dispensing Shipley LDD-26W developer. It also has a post-bake hotplate.

- STS: plasma-enhanced chemical vapor deposition (PECVD) system. Relatively low temperature (350°C) deposition of SiO_2 and Si_3N_4. Can use pieces or wafers up to 6".

- Raith 150: electron beam lithographic tool. Resolution around 50 nm routinely. 25 nm features have been reported. Stitching and overlay accuracy of ¡ 30 nm.

A.2 GLAM and McCullough equipment

- Focused ion beam (FIB): Strata Dual Beam 235 manufactured by FEI Company. Schottky field-emission electron source with energy dispersive spectrometry (EDS). Equipped with a gas injection system (GIS). Also contains an Omniprobe for in-situ transfers, usually of TEM samples.

- Scanning electron microscope (SEM): Sirion SEM manufactured by FEI Company. Schottky field-emission electron source with energy dispersive spectrometry (EDS). Resolution is between 1.5 nm at 10 kV and 2.5 nm at 1 kV.

- Kobe : DC sputtering chamber. Equipped with four 2" US MAK guns, and one 1" US miniMAK. All the 2" guns are shuttered and are tilted at 30 degrees from normal. The miniMAK has no shutter and is at normal incidence to the sample. All guns are located approximately 6" from the substrate. Equipped with a load-lock that is pumped by a turbo pump. The main chamber is pumped by a cryopump.

Appendix B

Detailed Parameters for Processing Stencil Samples

For parameters not explicitly given, see the specific instrument in appendix A.

B.1 wafer cleaning

- acetone
- methanol
- 2-propanol
- blow dry

B.2 Si_3N_4 membrane layer

- standard-clean on diffusion wet bench (wbdiff)
- grow 200 nm Si_3N_4 with Tylan nitride using recipe LONH378 (189 sccm; NH_3,189 sccm; 785 °C; 1 h).

B.3 Backside Si_3N_4 etch

- prime with HMDS in YES oven
- spin-on 1.7 μm AZ3612 using SVG coater for 30 s at 2000 rpm. No edge bead removal
- pre-exposure bake wafer for 2 min at 90 °C
- exposure with Karl Suss, 15 mW/cm^2 at 365 nm for 1.5-1.6 s
- develop in Shipley LDD26W using SVG developer program 6 (three development steps of 100 s each)
- post-develop bake for 2 min at 90°C
- Etch in Drytek 1, 5 min, 200 mTorr, 50 sccm SF_6, 33 sccm CF_3Br, RF Power 83 W
- clean in acetone, methanol, 2-propanol

B.4 lower contact layer

B.4.1 deposit resists

- prime with HMDS in YES oven
- spin-on 2 μm of LOL2000 on headway (3000 rpm, 60 s)
- bake 10 min at 170 °C on hotplate
- spin-on 1.0 μm AZ3612 using SVG coater for 30 s at 5500 rpm. Use edge bead removal for better contact with mask in exposure step
- pre-exposure bake wafer for 60 s at 90 °C

B.4.2 exposure

- clean mask (acetone, methanol, 2-propanol, blow dry)
- make sure the mask is oriented correctly
- exposure with Karl Suss, 15 mW/cm^2 at 365 nm for 1.0-1.1 s
- post-exposure bake 60 s on hotplate (115°C)

B.4.3 develop

- manually develop in LDD26W for 55 s. SVG developer does a very poor job for bilayer resist
- rinse in water for at least 2 min, blow dry
- hotplate, 1 min, 110°C

B.4.4 lower contact deposition

- deposit 2 nm Cr, 100 nm Pt in Metalica sputtering chamber

B.4.5 lift-off

- immerse in acetone for several hours. Use ultrasonic if needed but try to avoid
- methanol
- 2-propanol
- LDD-26W developer. Removes photoresist well, but can attack metals. However, it does not attack Pt. Initially used microposit remover 1165, developer works much better if compatible with the deposited metals
- acetone
- methanol

- 2-propanol
- blow dry

B.5 insulator and mask layer

- deposit 60 nm SiO_2 using STS (program: stohro60)
- deposit 10 nm Si_3N_4 using STS (program: stohrn10). Initial experiments initially deposited 1 nm Cr and 10 nm Pt on the Metallica sputter deposition chamber at this step

B.6 patterning of the SiO_2 layer

B.6.1 ebeam

- prime in YES oven
- spin-on PMMA (950k, 2%), 5000 rpm 40 s
- hot plate 180 °C, 2 min
- expose in RAITH (dot dose: 0.04 fC , area dose: 100 $\mu C/cm^2$)
- develop in 1:3 MIBK:2-propanol at 20 °C for 30 s
- rinse in 2-propanol for 30 s
- blow dry
- inspect wafer with SEM

B.6.2 RIE

- RIE Si_3N_4 mask. Drytek1, 33 sccm of CF_3Br, 50 sccm of SF_6. 200 mTorr. 83W
- etch SiO_2 in HF. BOE 20:1. 3 min

- inspect wafer with SEM

B.6.3 cleaning

- acetone
- methanol
- 2-propanol
- blow dry

B.7 Patterning of the magnetic layers

B.7.1 metal deposition and patterning

- DC sputter deposit magnetic layers. The exact layers depends on the particular sample. Pressure = 2 mTorr
- prime with HMDS in YES oven
- spin-on 1.7 μm AZ3612 using SVG coater for 30 s at 2000 rpm. No edge bead removal
- pre-exposure bake wafer for 2 min at 90 °C
- exposure with Karl Suss, 15 mW/cm^2 at 365 nm for 1.5-1.6 s
- develop in Shipley LDD26W using SVG developer program 6 (three development steps of 100 s each)
- post-develop bake for 2 min at 90°C
- Etch in MRC etcher, 115 min (depends on exact structure being etched), 4 mTorr of Ar, 15 sccm of Ar, RF Power 50 W
- clean in acetone, methanol, 2-propanol

- if necessary to finish cleaning resist, drytek O_2 plasma, 100 sccm, 150 mTorr, 65 W, 45 s

B.7.2 Si_3N_4 membrane etch

- deposit Apiezon W black wax on the front side of the wafer on a 130 °C hotplate
- etch in 22.5% KOH in Water at 70 °C for approx. 12 hours
- rinse in water
- strip the black wax in xylenes

Bibliography

[1] J. Stöhr, H.C. Siegmann: *Magnetism: From Fundamentals to Nanoscale Dynamics* (Springer, Berlin, To be published)

[2] F.J. Albert, J.A. Katine, R.A. Buhrman, D.C. Ralph: Applied Physics Letters **77**(23), 3809–3811 (2000)

[3] F. Albert, N. Emley, E. Myers, D. Ralph, R. Buhrman: Physical Review Letters **89**(22), 226 802–4 (2002)

[4] R. Nakajima: (1998), "X-ray magnetic circular dichroism spectroscopy in transition metal thin films", Ph.d., Stanford University

[5] H. Ohldag: (2003), "Exchange coupling of co and fe on antiferromagnetic nio investigated by dichroism x-ray absorption spectromicroscopy", Ph.D. thesis, University of Düsseldorf

[6] J. Stöhr, H.A. Padmore, S. Anders, T. Stammler, M.R. Scheinfein: Surf. Rev. Lett. (Singapore), Surface Review and Letters (1998)

[7] N. Mott: Proceedings of the Royal Society of London, Series A, Mathematical and Physical Sciences **153**(880), 699–717 (1936)

[8] N.F. Mott: Proceedings of the Royal Society of London, Series A, Mathematical and Physical Sciences **156**, 368–382 (1936)

[9] X. Waintal, E. Myers, P. Brouwer, D. Ralph: Physical Review B (Condensed Matter) **62**(18), 12 317–27 (2000)

[10] I. Campbell, A. Fert, A. Pomeroy: Philosophical Magazine **15**(137), 977–983 (1967)

[11] A. Fert, I. Campbell: Physical Review Letters **21**(16), 1190–2 (1968)

[12] T. Valet, A. Fert: Physical Review B-Condensed Matter **48**(10), 7099–7113 (1993)

[13] G. Busch, M. Campagna, P. Cotti, H.C. Siegmann: Physical Review Letters **22**(12), 597–599 (1969)

[14] P.M. Tedrow, R. Meservey: Physical Review Letters **26**(4), 192–195 (1971)

[15] P.M. Tedrow, R. Meservey: Physical Review B **7**(1), 318–326 (1973)

[16] A.G. Aronov: Zhurnal Eksperimental'noi i Teoreticheskoi Fiziki, Pis'ma v Redaktsiyu **24**(1), 37–9 (1976)

[17] A. Aronov: Zhurnal Eksperimentalnoi I Teoreticheskoi Fiziki **71**(7), 370–376 (1976)

[18] A. Aronov, G. Pikus: Fizika i Tekhnika Poluprovodnikov Soviet Physics - Semiconductors, June 1976; vol.10, no.6, p.698-700 **10**(6), 1177–80 (1976)

[19] M. Johnson, R.H. Silsbee: Physical Review Letters **55**(17), 1790–3 (1985)

[20] M. Johnson, R.H. Silsbee: Physical Review B (Condensed Matter) **37**(10, pt.A), 5326–35 (1988)

[21] R. Silsbee: Bulletin of Magnetic Resonance **2**, 284–285 (1980)

[22] M. Baibich, J. Broto, A. Fert, F. Vandau, F. Petroff, P. Eitenne, G. Creuzet, A. Freiderich, J. Chazelas: Physical Review Letters **61**(21), 2472–5 (1988)

[23] G. Binasch, P. Grunberg, F. Saurenbach, W. Zinn: Physical Review B **39**(7), 4828–4830 (1989)

[24] S.S.P. Parkin, R. Bhadra, K.P. Roche: Physical Review Letters **66**(16), 2152–2155 (1991)

[25] S.S.P. Parkin, Z.G. Li, D.J. Smith: Applied Physics Letters **58**(23), 2710–2712 (1991)

[26] J.C. Slonczewski: Journal of Magnetism and Magnetic Materials **159**(1-2), L1–L7 (1996)

[27] L. Berger: Physical Review B (Condensed Matter) **54**(13), 9353–8 (1996)

[28] Y. Bazaliy, B. Jones, S. Zhang: Physical Review B (Condensed Matter) **57**(6), R3213–16 (1998)

[29] J. Sun: Physical Review B (Condensed Matter) **62**(1), 570–8 (2000)

[30] M. Stiles, A. Zangwill: Physical Review B (Condensed Matter and Materials Physics) **66**(1), 014 407–14 (2002)

[31] E. Myers, D. Ralph, J. Katine, R. Louie, R. Buhrman: Science **285**(5429), 867–70 (1999)

[32] M. Tsoi, A. Jansen, J. Bass, W. Chiang, M. Seck, V. Tsoi, P. Wyder: Physical Review Letters **80**(19), 4281–4 (1998)

[33] J.A. Katine, F.J. Albert, R.A. Buhrman, E.B. Myers, D.C. Ralph: Physical Review Letters **84**(14), 3149–3152 (2000)

[34] P.C. van Son, H. van Kempen, P. Wyder: Physical Review Letters **58**(21), 2271–3 (1987)

[35] M. Johnson, R.H. Silsbee: Physical Review B (Condensed Matter) **35**(10), 4959–72 (1987)

[36] S. Hershfield, H. Zhao: Physical Review B (Condensed Matter) **56**(6), 3296–305 (1997)

[37] E. Rashba: Applied Physics Letters **80**(13), 2329–31 (2002)

[38] C. Heide, P. Zilberman, R. Elliott: Physical Review B (Condensed Matter) **63**(6), 064 424–7 (2001)

[39] L. Berger: Journal of Applied Physics **91**(10), 6795–800 (2002)

[40] J. Erskine, E.A. Stern: Physical Review B (Solid State) **12**(11), 5016–25 (1975)

[41] G. Schutz, W. Wagner, W. Wilhelm, P. Kienle, R. Zeller, R. Frahm, G. Materlik: Physical Review Letters **58**(7), 737–40 (1987)

[42] B.T. Thole, C. Paolo, F. Sette, G. van der Laan: Physical Review Letters **68**(12), 1943–6 (1992)

[43] P. Carra, B.T. Thole, M. Altarelli, W. Xindong: Physical Review Letters **70**(5), 694–7 (1993)

[44] J. Stöhr, R. Nakajima: IBM Journal of Research and Development **42**(1), 73–88 (1998)

[45] J. Stöhr, Y. Wu (Eds.): *New Directions in Research with Third-Generation Soft X-Ray Synchrotron Radiation Sources*, Vol. 254 of Nato ASI Series E (Kluwer Academic Publishers, Dordrecht, Netherlands, 1994), p. 221-50, Dordrecht, Netherlands, 1994)

[46] A. Morrish: *The physical principles of magnetism* (IEEE Press, New York, 2001)

[47] S.K. Kim, J.B. Kortright, S.C. Shin: Applied Physics Letters **78**(18), 2742–2744 (2001)

[48] Y. Wang, C. Jacobsen, J. Maser, A. Osanna: Journal of Microscopy-Oxford **197**, 80–93 (2000)

[49] U. Neuhausler, S. Abend, C. Jacobsen, G. Lagaly: Colloid and Polymer Science **277**(8), 719–726 (1999)

[50] A. Michette: *Optical Systems for Soft X-rays* (Plenum Press, New York/London, 1986)

[51] B. Winn, H. Ade, C. Buckley, M. Feser, M. Howells, S. Hulbert, C. Jacobsen, K. Kaznacheyev, J. Kirz, A. Osanna, J. Maser, I. McNulty, J. Miao, T. Oversluizen, S. Spector, B. Sullivan, Y. Wang, S. Wirick, H. Zhang: Journal of Synchrotron Radiation **7**, 395–404 (2000)

[52] C. Jacobsen, S. Williams, E. Anderson, M.T. Browne, C.J. Buckley, D. Kern, J. Kirz, M. Rivers, X. Zhang: Optics Communications **86**(3-4), 351–364 (1991)

[53] A.L.D. Kilcoyne, T. Tyliszczak, W.F. Steele, S. Fakra, P. Hitchcock, K. Franck, E. Anderson, B. Harteneck, E.G. Rightor, G.E. Mitchell, A.P. Hitchcock, L. Yang, T. Warwick, H. Ade: Journal of Synchrotron Radiation **10**, 125–136 (2003)

[54] S. Anders, H.A. Padmore, R.M. Duarte, T. Renner, T. Stammler, A. Scholl, M.R. Scheinfein, J. Stohr, L. Seve, B. Sinkovic: Review of Scientific Instruments **70**(10), 3973–3981 (1999)

[55] M. Stevens: *private communication*

[56] R. Koch, J. Katine, J. Sun: Physical Review Letters **92**(8), 088 302–4 (2004)

[57] J. Lee: Optical Engineering **25**(5), 636–43 (1986)